



Co-precipitation strengthening behavior on paint-baked Al–Mg–Si–Cu aluminium alloys under combined pre- and natural ageing

Wei-Yi Yang^a, Ching-Wen Yeh^a, Seiichiro Ii^b, R. Devesh Kumar Misra^c, Po-Kai Chiu^d, Tsai-Fu Chung^{a,*}

^a Department of Materials Science and Engineering, National Yang Ming Chiao Tung University, Hsinchu, Taiwan

^b National Institute for Materials Science, Sengen 1-2-1, Tsukuba, 305-0047, Japan

^c Department of Biomedical Engineering and Department of Mechanical, Robotics and Industrial Engineering, Lawrence Technological University, 21000 West Ten Mile Road, Southfield, MI, 48075, USA

^d National Institutes of Applied Research, National Center for Instrumentation Research, Taiwan

ARTICLE INFO

Keywords:

Al–Mg–Si–Cu aluminum alloys
Pre-ageing
Prolonged natural ageing
Paint-baking
Multiphasic Co-precipitation
Strain-induced selective nucleation mechanism

ABSTRACT

Optimizing the interplay between pre-ageing (PA), natural ageing (NA), and paint-baking (PB) is critical for enhancing the precipitation hardening of Al–Mg–Si–Cu alloys. This study investigates the multiphase precipitation kinetics in an Al–0.7Si–0.9Mg–0.2Cu (wt%) alloy subjected to PA (80 °C for 1 h), varying NA durations (1–30 days), and PB (180 °C for 30 min). By combining synchrotron small-angle X-ray scattering (SAXS) with high-resolution transmission/scanning electron microscopy (TEM/STEM) characterization, we reveal two governing mechanisms responsible for the superior mechanical performance. First, prolonged NA (30 days) promotes the atomic-scale ordering of GP zones. Initially disordered clusters evolve into ordered configurations containing Si/Cu-rich layers, effectively reducing the thermodynamic barrier for β''/β' precipitation during subsequent baking. Second, we elucidate a strain-induced selective nucleation mechanism for θ'/Q' phases along dislocations. Continuous solute segregations transition into segmented precursors, where only variants satisfying crystallographic matching conditions undergo growth into discrete precipitates. This hierarchical microstructure, comprising dense β''/β' in the matrix and discrete θ'/Q' along dislocations, enhances both strength and ductility. The optimized processing yields an ultimate tensile strength of ~ 249 MPa with excellent ductility ($\sim 19.6\%$), demonstrating that the strategic application of prolonged NA can effectively tailor precipitate architecture in Al–Mg–Si–Cu alloys.

1. Introduction

The treatments of pre-ageing (PA) and paint-baking (PB) have been recognized as an effective strategy to mitigate the adverse effects of extended room-temperature storage on the Al–Mg–Si–Cu alloys [1–3]. After undergoing cold or hot rolling, Al–Mg–Si–Cu alloy sheets are subjected to a supersaturated solid solution heat treatment (SSSS), followed by natural ageing (NA), and then a subsequent paint-bake (PB) treatment at ~ 185 °C for 30 to 40 min [4–6]. The precipitation sequence of Al–Mg–Si–Cu aluminum alloys is generally involved: SSSS [7–9] \rightarrow Mg/Si–Cu rich solute clusters [10–12] \rightarrow GP zones [13,14] \rightarrow β'' , L/Q', S, C/QP/QC, θ' , U1 [15–17] \rightarrow β' , Q', θ [11] \rightarrow β , Si particles [18,19]. It has been reported that natural ageing, regardless of duration from short-term (≤ 1 day) to prolonged periods (from 30 days up to 1 year),

significantly impedes the precipitation kinetics of β'' ($\text{Mg}_{6-x}\text{Al}_{1+x}\text{Si}_4$, $x = 0$ to 2) or β' (Mg_9Si_5) phases, which are the primary strengthening precipitates formed during artificial peak ageing (i.e., 180 °C for 12 h to 36 h) [18–21]. Moreover, several investigations [18,20,21] have indicated that elevated pre-ageing temperature (≥ 100 °C) stabilizes β'' -type precursor GP zones and promotes their transformation into strengthening β''/β' phases during the subsequent paint-baking treatment. In our earlier study on Al–0.7Si–0.9Mg–0.2Cu (wt.%) alloys, subjected to PA at 80 °C for 1 h, NA for 14 days, and PB at 180 °C for 30 min [22], it shows that the co-precipitation of β''/β' and θ'/Q' phases resulted in an ultimate tensile strength (UTS) of ~ 223 MPa and good ductility of $\sim 29\%$. Nevertheless, whether the cumulative effects of low-temperature PA and prolonged NA can tailor precipitation kinetics of β'' -type precursor GP zones, β''/β' phases, and θ'/Q' phases, thereby enabling controlled

* Corresponding author.

E-mail address: tfchung@nycu.edu.tw (T.-F. Chung).

<https://doi.org/10.1016/j.jmrt.2026.02.065>

Received 23 December 2025; Received in revised form 1 February 2026; Accepted 8 February 2026

Available online 10 February 2026

2238-7854/© 2026 The Author(s). Published by Elsevier B.V. This is an open access article under the CC BY-NC-ND license (<http://creativecommons.org/licenses/by-nc-nd/4.0/>).

multiphasic co-precipitation, remains to be understood.

In a previous investigation on Al-0.62Mg-0.93Si (wt.%) aluminum alloys [10], the atom probe tomography (APT) analysis shows the effect of short-term (30 h) and prolonged (325 days) NA treatments directly after solid solution treatment on the clustering behavior. It is suggested that Mg atoms gradually diffuse into pre-existing Si-rich clusters, which are formed in the short-term NA (30 h), and result in the formation of more ordered Mg/Si-rich GP zones with a Mg/Si ratio below unity during the prolonged NA (325 days) [10]. Those ordered Mg/Si-rich GP zones with a diameter of ~ 1.2 nm are recognized as non- β'' type GP-zones and are unlikely to transform into β''/β' during the subsequent PB treatment [4,10]. On the other hand, replacing NA by PA at 90 °C for 5 h after solid-solution treatments has been reported to promote the formation of GP zones [10]. These GP zones with more uniform Mg/Si ratios (~ 1.0) are presumed to develop into β'' after paint-bake treatment, increasing hardness [10]. It has also been reported in a recent study on Al-0.85Si-0.75Mg-0.7Cu-0.3Mn aluminum alloys that the PA treatment directly after solid-solution treatment enhances the formation of β'' -type precursor GP-zones [4]. In an investigation on Al-0.70Mg-0.85Si-0.15Fe-0.25Mn (wt.%) aluminum alloys subjected to PA (90 °C for 24 h) directly after solid-solution treatment [13], a combination of low-angle annular dark-field scanning transmission electron microscopy (LAADF-STEM) and first-principles density functional theory (DFT) reveals the atomic structures of β'' -type precursor GP-zones for the first time. These GP zones consist of 3–4 eye-like subunits per unit under d scanning transmission electron microscopy (STEM) observation along the $[100]_{\text{Al}}$ zone axis [13]. The density functional theory (DFT) calculations further indicate that the development of such eye-like subunits significantly increases the thermal stability of β'' -type precursor GP-zones [13]. A higher number of eye-like subunit structures in β'' -type precursor GP-zones is presumed to be a more effective nucleation site for β''/β' phases during subsequent artificial ageing [13]. In an investigation on Al-0.65Mg-0.81Si-0.16Fe-0.05Cu (wt.%) aluminum alloys subjected to PA at 100 °C for 1 h to 400 h directly after solid-solution treatment [18], it has been revealed that the effect of various PA durations on the precipitation behavior. The size, fraction, and composition evolution of β'' -type precursor GP zones are characterized by STEM imaging and STEM energy-dispersive X-ray spectroscopy (EDS). At 1 h PA treatment, nanoscale clusters (1.0–1.5 nm) with broad Mg/Si ratios (average ~ 0.82) are observed, suggesting an early-stage compositional disorder [18]. With PA extended beyond 10 h, the number density of clusters increases, accompanied by transformation into spherical β'' -type precursor GP zones with a size of 1.0–1.5 nm and a narrowly distributed Mg/Si ratio (average ~ 1.0) [18]. At 400 h PA treatment, it has been reported that the concurrent growth and structural ordering of both precursor GP zones and β'' precipitates are associated with an increase in yield strength, reaching ~ 272 MPa [18]. Despite these insights, during the prolonged PA treatment, the structural role of eye-like subunits in the precursor-to-precipitate transition remains unclear. Whether the low-temperature PA treatment combined with prolonged natural ageing can enhance the formation and growth of β'' -type precursor GP zones remains to be investigated. Moreover, it is of interest to further explore the morphology transition of spherical-like β'' -type precursor GP zones to rod-like β'' precipitates. This morphological transformation of GP zones to β'' phases remains an unresolved issue analogous to the unclear evolution pathway of spherical GPI zones to plate-like GPII zones in Al–Zn–Mg–Cu aluminum alloys [23–25].

In a recent work on the Al-1.1Si-0.68Mg-0.58Mn (wt.%) aluminum alloys [20], the effect of short-duration, high-temperature PA on the subsequent precipitation behavior during the NA and PB treatment has been reported. It has been found that introducing a short-duration PA treatment (185 °C for 5 min) at the same PB temperature between the solution heat treatment and subsequent prolonged NA (30 days) significantly increases the formation of β'' -type precursor GP-zones, which exhibit more than six eye-like subunits [20]. After PB treatment

(185 °C for 4 h), the β'' -type precursor GP zones have been observed to grow parallel to the β'' growth directions of $[230]_{\text{Al}}$ and $[130]_{\text{Al}}$ axes [20]. Therefore, an increased volume fraction of β'' -type precursor GP zones and β'' precipitates concurrently enhances both ultimate tensile strength (~ 325 MPa) and ductility ($\sim 18\%$) [20]. On the other hand, in that work [20], non-PA samples (i.e., subjected to prolonged NA (30 days) directly followed by PB at 185 °C for 6 h) exhibit a relatively lower UTS (~ 296 MPa) and ductility ($\sim 13\%$) [20]. It can be presumed that the 30 days of prolonged NA can only form non- β'' type GP-zones, thereby requiring a higher energy barrier to transform into strengthening β'' phases. It remains an intriguing question whether the combination of low-temperature PA (≤ 100 °C) and prolonged NA (≥ 30 days) can effectively promote the formation of β'' -type precursor GP zones or β' -like precipitates. In another investigation on Al-0.9Si-0.70Mg-0.42Mn-0.08Cu-0.05Zn (wt.%) aluminum alloys [21], it has been revealed that a combined treatment of PA at 210 °C for 40 min and PB at 180 °C for 30 min can obtain a significantly higher UTS of ~ 320 MPa but a lower elongation of $\sim 7.8\%$. This enhancement in strength is attributed to accelerated precipitation kinetics at an elevated PA temperature, facilitating the rapid nucleation and growth of β'' -type precursor GP zones and β'' phases [21]. However, the high temperature and increased solute diffusivity near grain boundaries supposedly promote the formation of large β phases, which become stress-concentrated regions and intergranular crack initiation sites, leading to a loss in elongation ($\sim 7.8\%$) [21]. On the other hand, an investigation on Al-0.9Mg-0.7Si-0.2Cu-3.0Zn (wt.%) aluminum alloys [14] reveals the effects of the Zn addition and the slow cooling rates (i.e., 0.2, 0.3, and 0.4 °C/min) after PA treatment (i.e., 80 °C for 1 h) on the precipitation kinetics during prolong NA (1, 60, and 180 days). The combined effects stabilize the β'' -type precursor GP zones and promote complete solute diffusion, ultimately offering a favorable environment for β'' nucleation [14]. Whether the Cu addition would reduce the formation energy barrier of both β'' -type precursor GP zones and β'' phases has yet to be investigated. In the 2000 (Al–Cu–Mg(Li)), 6000 (Al–Mg–Si–Cu), and 7000 (Al–Zn–Mg–Cu) aluminum alloys, thermo-mechanical processing prior to solid solution and ageing treatments, such as high-temperature upsetting-extrusion [26–28] and cold/hot rolling [22,29,30], plays an important role in controlling the grain structures and mechanical properties. Recently, combined thermo-mechanical and ageing processes, including prior strain [31–33], warm forming [34], creep-age forming [25,35,36], and intermediate cold deformation [37–39], have been shown to promote dynamic precipitation, thereby mitigating the strength-ductility trade-off effectively. Although the high stacking fault energy of aluminum alloys easily promotes dynamic recovery, short-duration solid solution treatments often fail to fully eliminate deformation-induced defects, leaving retained dislocations in the aluminum matrix. Studies on Al-0.6Mg-0.6Si-0.3Fe-0.15Zn-0.1Cu (wt. %) [40], Al-0.5Si-0.6Mg-0.2Fe-0.003Cu (wt.%) [26], and Al-0.6Mg-0.3Si-0.35Fe-0.3Mn-0.7Cu (wt.%) [27] have indicated that the severe extrusion followed by artificial ageing promotes a synergistic effect of grain refinement and dynamic precipitation strengthening. Adamczyk-Cieslak et al. [40] have revealed the effect of hydrostatic and torsion extrusions, both followed by ageing at 175 °C for 15 h, on the precipitation of β''/β' and β phases. The hydrostatic extrusion induces a homogeneous dislocation distribution that promotes a higher fraction of fine β''/β' phases [40]. Conversely, a torsional deformation generates inhomogeneous and distorted dislocation configurations, facilitating partial dissolution of β''/β' phases and promoting the transformation into β phases [40]. H. J. Roven et al. [26] have shown that multiple equal channel angular extrusion (ECAE) passes followed by artificial ageing at 175 °C for 48 h bring about a bimodal hardness response in aged Al-0.5Si-0.5 Mg alloys. The first hardness peak is attributed to the formation of dislocation-enhanced β'' phases, whereas the second hardness peak is ascribed to the phase transformation of β'' to β' phases [26]. Following ECAE and ageing processing, β'' precipitates exhibit a

fragmented morphology as they preferentially and discretely nucleate along dislocations [26]. Such sparsely-distributed β'' precipitates are proposed to enhance the chance of precipitate-precipitate interactions and increase local lattice strain during growth, thereby promoting phase transformation of β'' into β' . Those thermo-mechanical and ageing processes presumably introduce hard and soft domains, such as β''/β' -rich regions or dislocation-dense networks, that bring about higher local stresses, whereas the surrounding softer α -Al matrix accommodates most of the plastic strain near the phase boundaries. Whether the hard and soft domains can be incorporated into the deep-learning-crystal-plasticity model [41] to predict the evolution of stress-strain partitioning on precipitation and the resulting tensile properties in Al–Mg–Si–Cu alloys remains an open question. In our recent investigation on Al-8.9Zn-2.2Mg-2.1Cu (wt%) aluminum alloys [28], we have revealed that high-temperature upsetting-extrusion before short-duration solid solution treatment (i.e., 3 h) and artificial ageing (i.e., @ 120 °C for 12 h) plays a critical role in tailoring grain structure and co-precipitation. A higher density of retained dislocations not only facilitated the formation of recrystallized grains during the solid solution treatment, but also enhanced the nucleation of η'/η and Y-phase precipitates during artificial ageing, resulting in dynamic Hall-Petch strengthening and precipitate hardening [28]. Furthermore, in our early investigation on Al-0.7Si-0.9Mg-0.2Cu (wt.%) aluminum alloys [22], it shows that the presence of retained dislocations, introduced by 50% hot rolling and followed by a short-duration multistep solid solution treatment, enhances the diffusion of Cu atoms during a sequential thermal ageing process. The increased atomic mobility of Si, Mg, and Cu, driven by both dislocation-enhanced pathways and paint-baking treatments, facilitates the formation of β''/β' phases in the aluminum matrix and the co-precipitation of Cu-rich θ' (Al_2Cu) and Q' ($\text{Al}_4\text{Cu}_1\text{Mg}_8\text{Si}_7$ or $\text{Al}_{3.8}\text{Cu}_1\text{Mg}_{8.6}\text{Si}_7$) phases along dislocation structures [22]. A similar phenomenon has been reported in Al-0.78Mn-0.81Mg-1.0Si (wt.%) aluminum alloys [42], where high-resolution TEM and EDS analyses revealed that triple junction grain boundaries and partial dislocations associated with stacking fault structures promote the diffusion of Al, Mn, and Si, leading to the formation of nanoscale precipitates. Furthermore, in-situ transmission electron microscopy (TEM) and atomistic simulations under high-density electric current have shown that dislocation and grain-boundary dislocation networks can be selectively activated, and act as fast paths for atomic transport and precipitate formation [43]. The synergistic effect of β''/β' and θ'/Q' precipitation strengthening contributed to a significantly improved UTS of ~ 223 MPa and good ductility of $\sim 29\%$ [22]. These findings are consistent with the previous work [19], where co-precipitation of β''/Q' is observed along dislocation segments following artificial ageing at 220 °C for 4 h. In that case, the lower Cu content likely inhibited the nucleation of θ' phases, while the elevated ageing temperature readily induced Q' phase precipitation [22]. Moreover, a recent investigation on hot-rolled Al-4.9Cu-0.74Mg-0.51Si-0.48Mn (wt%) aluminum alloys, subjected to solid-solution treatment at 500 °C for 1 h and prolonged artificial ageing at 170 °C for 96 h [44], reveals that the retained dislocations are covered with interconnected co-precipitates, mainly comprising θ' (Al_2Cu) and S (Al_2CuMg) phases. It remains unclear whether, in Al–Mg–Si–Cu aluminum alloys, retained dislocations, as coupled with sequential PA, NA, and PB, could facilitate solute diffusion, thereby affecting the evolution of precursor GP zones, β'' , or other secondary strengthening phases. This interplay among dislocation structures, precipitation behavior, and mechanical properties requires further systematic investigation.

Based on the above review, the cumulative effects of pre-ageing (PA) and prolonged natural ageing (NA) on the multiphase co-precipitation in paint-baked AA6061 (Al–Mg–Si–Cu) alloys remain insufficiently understood. In particular, it is still unclear whether prolonged NA promotes the nucleation and longitudinal growth of precursor GP zones, how these GP zones subsequently transform into β''/β' phases, and to

what extent they contribute to the formation of secondary hardening precipitates such as Q' and θ' during PB. To address this knowledge gap, we employ an integrated characterization approach that combines synchrotron small-angle X-ray scattering (SAXS) with high-resolution transmission electron microscopy (TEM) and scanning transmission electron microscopy (STEM) to quantitatively analyze the size, number density, and volume fraction of coexisting GP, β''/β' , and θ'/Q' precipitates at different PA-NA-PB stages. These microstructural observations are systematically correlated with tensile properties to clarify the dominant strengthening mechanisms and to refine the understanding of the paint-baked hardening response. This study presents a mechanistic framework for utilizing tailored PA-NA-PB sequences to engineer controlled multiphase co-precipitation and enhance the strength and ductility of AA6061 alloys.

2. Experimental procedure

2.1. Composition and heat treatment

The AA6061 aluminum alloy sheets (Al-0.7Si-0.9Mg-0.2Cu-0.5Fe-0.2Cr-0.1Mn, wt%) used in this study were supplied by Hing Chun Yit (HCY) Inc., Taiwan. The same samples were employed in our previous work [22]. The as-cast ingots were homogenized at 550 °C for 72 h and subsequently hot-rolled at 450 °C to a final thickness of approximately 3 mm, corresponding to a 50% reduction. The rolled sheets were then subjected to a three-step supersaturated solid solution treatment (SSSS) at 495 °C, 510 °C, and 540 °C, each held for 15 min, followed by water quenching to room temperature (25 °C). It was shown to effectively dissolve pre-existing coarse precipitates and maximize solute supersaturation while avoiding incipient melting. A pre-ageing (PA) treatment at 80 °C for 1 h was applied to SSSS samples, followed by furnace cooling to room temperature. After PA, three natural ageing (NA) durations at 25 °C for 1 day, 7 days, and 30 days were employed, producing Samples #1, #3, and #5, respectively. These NA durations were selected to represent realistic storage intervals between forming and painting for electric vehicle (EV) body panels and smartphone housings, ranging from short in-line processing (1 day) to weekly (7 days) and long-term inventory or shipment (30 days). These samples were then subjected to a paint-baking (PB) treatment at 180 °C for 30 min (i.e., a standard automotive paint-bake cycle for 6000 series aluminum alloys), resulting in Samples #2, #4, and #6, respectively. A schematic illustration of the entire heat treatment route and sample labeling is presented in Fig. 1.

2.2. Mechanical tensile deformation

Vickers Hardness tests were performed on the Samples #1 to #4 with a TAIMECO THV-2100 hardness testing machine. The value of hardness was measured using a load of 200 gf. The load application time for one indentation was 10 s, and the average hardness value for each specimen was determined from 25 tests on the corresponding sample. For the mechanical properties, we prepared three tensile test samples for the four ageing conditions to measure the yield strength, the UTS, and the

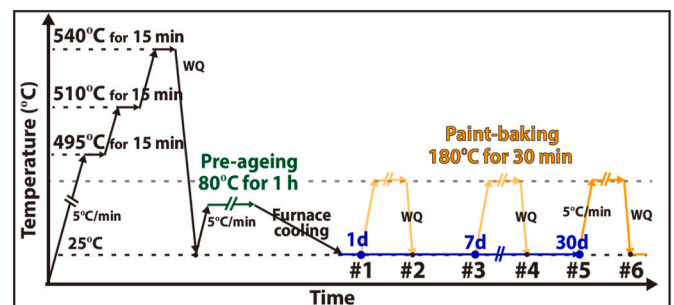


Fig. 1. The schematic diagrams of heat treatment in the present work.

strain under the 800 Series Advanced Universal Electromechanical Materials Testing Machines Model 869 (50 kN) with a strain rate of 10^{-3} s^{-1} . The tensile test samples were prepared based on ASTM E8.

2.3. Microstructure characterization

The SAXS (small-angle X-ray scattering) measurements were performed at the BL23A and TPS13A beamlines of the National Synchrotron Radiation Research Center (NSRRC), Taiwan, with high-flux collimated X-rays of 15 keV and a beam diameter of $\sim 500 \mu\text{m}$. The SAXS samples were prepared into $\sim 5 \text{ mm} \times \sim 5 \text{ mm} \times \sim 420 \mu\text{m}$ and measured under a collection time of 10 min for optimal transmission of X-rays. In the SAXS work, we focused on all samples to evaluate precipitate evolution. The collected 2D SAXS patterns were circularly averaged according to the standard procedure and reduced to the 1D SAXS curves as a function of scattering vector $Q = \frac{4\pi \sin(\theta/2)}{\lambda}$, where Q is the scattering vector, θ is the scattering angle and λ is the incident X-ray wavelength. For clarity, all symbols and abbreviations appearing in the equations are illustrated in Table A1 (Appendix).

TEM specimens were prepared by cutting discs from Samples #1 to #4 and thinning them to a thickness of about $75 \mu\text{m}$ before they were twin-jet electropolished in a mixture of 33% nitric acid and 67% methanol at -25°C at a voltage of 12–15 V. Moreover, the oxidation layers and the hydrocarbon contamination of the pre-observed TEM specimens were presumably eliminated by an M1040 NanoMill TEM specimen preparation system (E.A. Fischione Instruments) and an M1070 Nanoclean plasma cleaner (E.A. Fischione Instruments). Next, HR-TEM and atomic HAADF-STEM observations were performed with JEOL JEM-F200 microscope (National Yang Ming Chiao Tung University, NYCU) and Cs-corrector FEI Titan Chemi-STEM microscope (National Center for Instrumentation Research), respectively. The HAADF-STEM images were recorded with a detector at the collecting angle range of $\sim 35.9 \text{ mrad}$ (inner angle) to $\sim 143.6 \text{ mrad}$ (outer angle). Additionally, the HR-TEM and HAADF-STEM images were partially noise filtered and subjected to inverse fast Fourier transformation (FFT) reconstruction using appropriately selected reflection spots from the FFT diffractogram, which enhanced the Z-contrast and phase contrast, respectively.

3. Results

3.1. Mechanical properties

Fig. 2 shows the stress-strain curves for Samples #1 to #6. Table 1 summarizes the mechanical properties, including hardness, yield strength, ultimate tensile strength (UTS), and elongation, for each ageing condition. For the samples that underwent only pre-ageing (PA) and natural ageing (NA) without subsequent paint-baking (PB) (i.e., Samples #1, #3, and #5), a gradual increase in strength was observed with the NA duration. The yield strength improved from $63 \pm 4 \text{ MPa}$ (#1), $69 \pm 3 \text{ MPa}$ (#3), to $93 \pm 2 \text{ MPa}$ (#5), while UTS increased from $161 \pm 4 \text{ MPa}$ (#1), $167 \pm 3 \text{ MPa}$ (#3), to $187 \pm 2 \text{ MPa}$ (#5). The corresponding hardness also rose from $54 \pm 2 \text{ HV}$ (#1), $55 \pm 3 \text{ HV}$ (#3), to $64 \pm 3 \text{ HV}$ (#5). The gradual increase in mechanical strength and hardness is presumably associated with the growth of solute clusters or GP zones during NA. Whether the prolonged NA duration up to 30 days (Samples #5) enhances the transformation of GP zones has yet to be revealed. Alternatively, the increase in mechanical strength leads to a decrease in ductility from $36.4 \pm 3.1\%$ (#1) to $28.0 \pm 2.7\%$ (#3) and further to $21.7 \pm 2.0\%$ (#5), suggesting a growing strength-ductility trade-off. The beneficial effects of the PB treatment are evident for Samples #2, #4, and #6 across all NA durations. The Sample #2, which undergoes the same PA and NA duration but is followed by an additional PB treatment (PA + 01dNA + PB), exhibits a substantial improvement in strength: hardness increases to $86 \pm 2 \text{ HV}$, yield strength to 115 ± 2

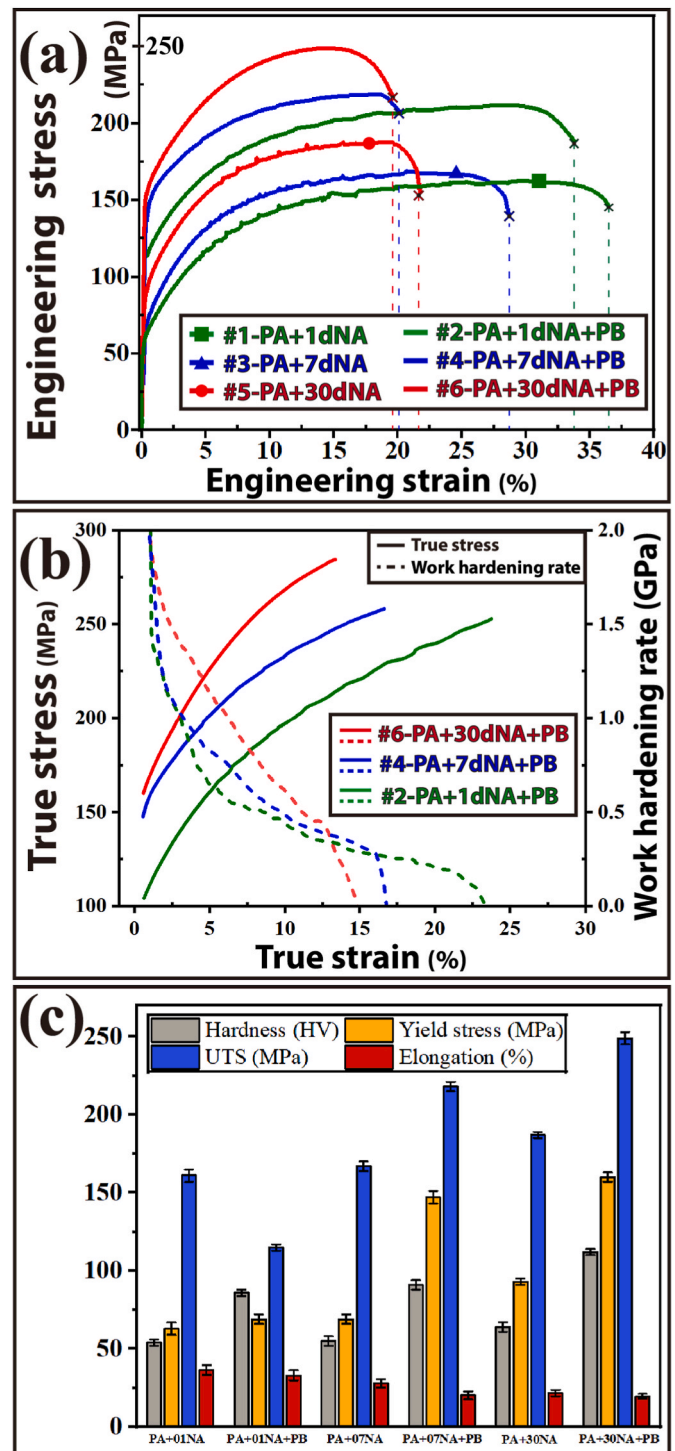


Fig. 2. (a) The engineering stress-strain curves of AA6061 alloy subjected to different heat treatment conditions (i.e., Samples #1 to 6). (b) The true stress-strain curves and corresponding work-hardening rate of the samples with different natural durations but the same paint-baking treatment. (c) Summary chart of the mechanical properties of Samples #1 to #6.

MPa, and UTS to $211 \pm 2 \text{ MPa}$. However, this enhancement is accompanied by a slight loss in ductility, as the elongation decreased to $33.7 \pm 3.2\%$. Sample #4 (PA + 07dNA + PB) exhibits a hardness of $91 \pm 3 \text{ HV}$, yield strength of $147 \pm 4 \text{ MPa}$, and UTS of $218 \pm 3 \text{ MPa}$. Sample #6 (PA + 30dNA + PB) shows the highest strength among all: hardness of $112 \pm 2 \text{ HV}$, yield strength of $160 \pm 3 \text{ MPa}$, and UTS of $249 \pm 4 \text{ MPa}$. Notably, despite the dramatic improvement in strength of Sample #6,

Table 1
The mechanical properties of Samples #1 to #6 in this present work.

Samples	Heat Treatment	Hardness (HV)	Yield stress (MPa)	UTS (MPa)	Elongation (%)
#1	PA + 01dNA	54 ± 2	63 ± 4	161 ± 4	36.4 ± 3.1
#2	PA + 01dNA + PB	86 ± 2	115 ± 2	211 ± 2	33.7 ± 3.2
#3	PA + 07dNA	55 ± 3	69 ± 3	167 ± 3	28.0 ± 2.7
#4	PA + 07dNA + PB	91 ± 3	147 ± 4	218 ± 3	20.2 ± 2.5
#5	PA + 30dNA	64 ± 3	93 ± 2	187 ± 2	21.7 ± 2.0
#6	PA + 30dNA + PB	112 ± 2	160 ± 3	249 ± 4	19.6 ± 1.5

the elongation of $(19.6 \pm 1.5\%)$ does not show significant deterioration compared to Sample #4 ($20.2 \pm 2.5\%$) and Sample #5 ($21.7 \pm 2.0\%$). Fig. 2b presents the true stress-strain curves and corresponding work-hardening rate profiles for three PB-treated samples: #2 (PA + 01dNA + PB), #4 (PA + 07dNA + PB), and #6 (PA + 30dNA + PB). Among the three conditions, Sample #6 clearly exhibits the highest true stress throughout the plastic deformation range. The peak true stress of Sample #6 approaches ~ 290 MPa (at a true strain of $\sim 15\%$), surpassing that of Sample #4 (~ 260 MPa at a true strain of $\sim 17\%$) and Sample #2 (~ 260 MPa at a true strain of $\sim 26\%$). The work-hardening rate also reflects this trend, with Sample #6 maintaining higher hardening capacity at comparable strain levels. This suggests a more effective and stable distribution of strengthening precipitates under the extended

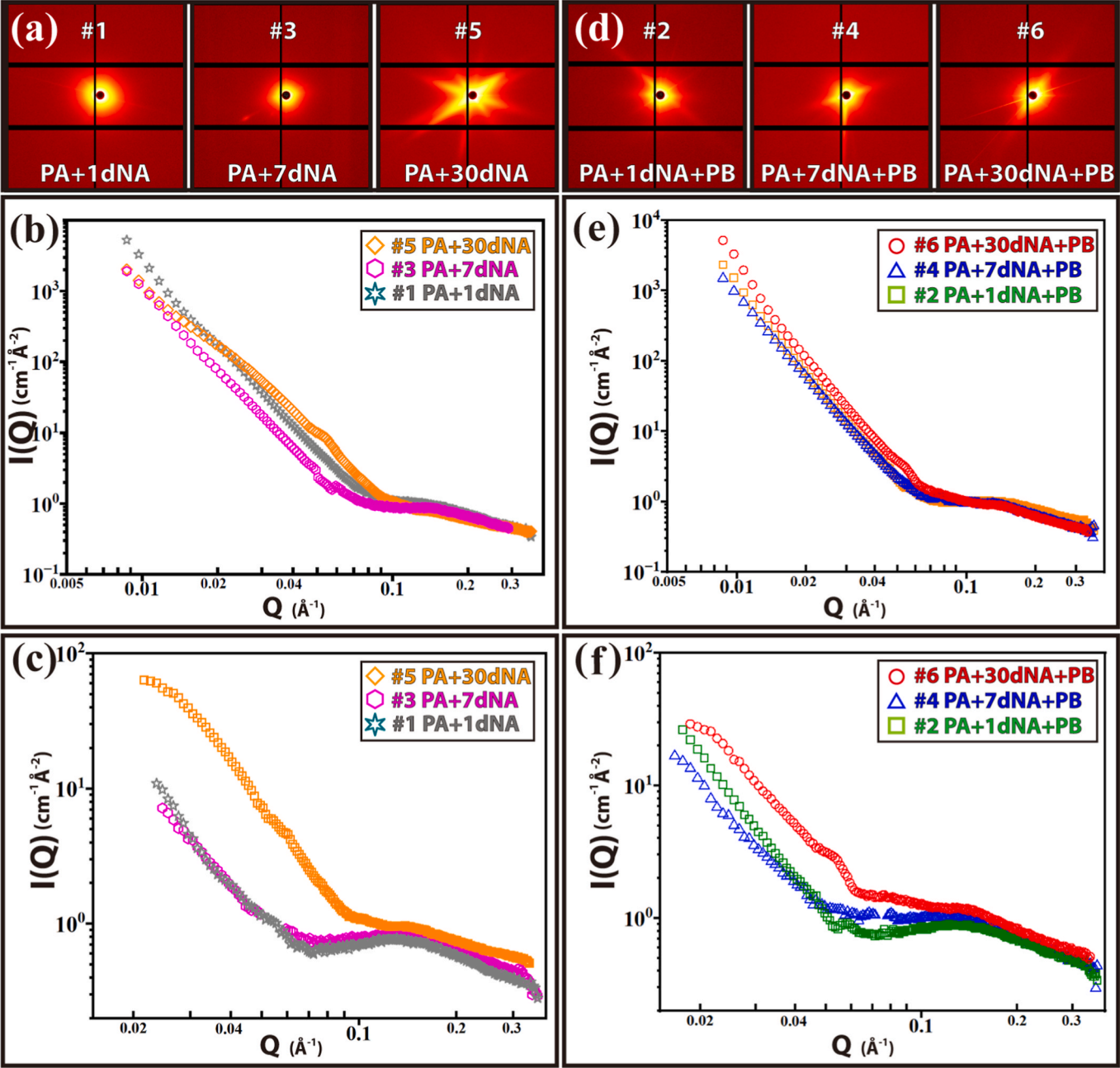


Fig. 3. (a, d) 2D SAXS patterns of non PB-treated (#1, #3, and #5) and PB-treated samples (#2, #4, and #6), respectively. (b, e) Reduced 1D SAXS profiles of non PB-treated (#1, #3, and #5) and PB-treated samples (#2, #4, and #6), respectively. (c, f) 1D SAXS profiles of non PB-treated (#1, #3, and #5) and PB-treated samples (#2, #4, and #6) after the power-law subtraction in the low-Q region to exclude the effect of large second-phase particles in the micrometer scale, respectively.

ageing and baking sequence.

3.2. Quantitative structural characterization of precipitates

The two-dimensional (2D) small-angle X-ray scattering (SAXS) patterns of Samples #1 to #6 under various natural ageing (NA) and paint-bake (PB) conditions are shown in Fig. 3a and d. Fig. 3a displays the 2D SAXS patterns of the non-PB-treated samples, i.e., PA + 1dNA (#1), PA + 7dNA (#3), and PA + 30dNA (#5), while Fig. 3d shows the corresponding PB-treated counterparts, PA + 1dNA + PB (#2), PA + 7dNA + PB (#4), and PA + 30dNA + PB (#6). The transition of 2D SAXS patterns from isotropic to anisotropic rings, accompanied by changes in both size and shape of streaking features, such as their dimension, thickness, and length, can be attributed to the morphological evolution of large second-phase particles, solute clusters, and nanoscale precipitates. Fig. 3b and e presents the corresponding one-dimensional (1D) SAXS intensity profiles, $I(Q)$, as a function of the scattering vector (Q), obtained by data reduction and radial integration of the 2D patterns in Fig. 3a and d, respectively. In Fig. 3b and e, the upturned intensity in the low- Q region (i.e., $0.008 \text{ \AA}^{-1} < Q < 0.035 \text{ \AA}^{-1}$) exhibits a characteristic power-law scattering behavior, described by $I(Q) \propto Q^{-\alpha}$, with a slope of approximately $\alpha \approx 4$. This scattering regime is typically associated with Porod's law, which suggests the presence of large, well-defined second-phase particles with sharp boundaries or interfaces [28,45–47]. These second-phase particles may include primary Fe-rich intermetallic compounds or coarse Mg_2Si particles, which are either retained from the solidification stage or insufficiently dissolved during the homogenization treatment [22]. The contribution of these large-scale particles with smooth surfaces is more pronounced in the low- Q region due to their large size, but their effect is generally considered extrinsic to the precipitation strengthening process. In Fig. 3c and f, we have subtracted the respective power-law-fitted intensity from the low- Q intensity to remove the effect caused by large second-phase particles, generally resulting in two Guinier shoulder of form factors in the middle- ($\sim 0.02 \text{ \AA}^{-1} < Q < 0.06 \text{ \AA}^{-1}$) to high- Q region ($\sim 0.15 \text{ \AA}^{-1} < Q < 0.35 \text{ \AA}^{-1}$), respectively, for Sample #1 to #6. For the Samples #1 to #4, the SAXS intensities in the middle- Q region (i.e., $\sim 0.025 \text{ \AA}^{-1} < Q < \sim 0.060 \text{ \AA}^{-1}$) show the power-law scattering behavior of the exponent $\alpha = 2$. The exponent of 2 indicates a disk-like morphology of second-phase particles [22,46]. Additionally, the high- Q intensity profiles ($0.15 \text{ \AA}^{-1} < Q < 0.35 \text{ \AA}^{-1}$) of Samples #1 to #4 display a shoulder or peak (at $\sim 0.15 \text{ \AA}^{-1}$) followed by a power-law intensity decay with an exponent $\alpha = 1$. This indicates the presence of rod-shaped nanoscale structures embedded in the matrix. Therefore, it can be concluded that the subtracted SAXS intensity profiles of Samples #1 to #4 are contributed by disk-like and rod-like particles/clusters with large discrepancies in sizes, respectively. The middle- Q intensity profile is mainly contributed by disk-like particles. The high- Q intensity profile is mainly contributed by small rod-like cluster/GP zones. Those SAXS intensity profiles, $I(Q)$, can be expressed by the sum or combination of the SAXS intensities contributed by disk-like particles, $I_{\text{disk}}(Q)$, and rod-like clusters/GP zones, $I_{\text{rod}}(Q)$, respectively, as given by

$$I(Q) = I_{\text{disk}}(Q) + I_{\text{rod}}(Q) \quad (1)$$

$I_{\text{disk}}(Q)$ or $I_{\text{rod}}(Q)$ is modelled by the product of the cylinder form factor model with the Schultz size distributions and hard-sphere structure factor $S(\eta, Q)$ [48,49], considering hard-sphere interaction between particles [47]. For clarity, all symbols and abbreviations appearing in the equations are illustrated in Table A1 (Appendix). The poly-dispersed disks with a radius (R) and the Schulz distribution $f(T)$ of thickness (T), produce the intensity profile as given by

$$I_{\text{disk}}(Q) = \eta \Delta \rho^2 \iint V_p^2 S(\eta, Q) f(T) j_0 \left(\frac{T}{2} \cos \alpha \right)^2 \left[\frac{2J_1(QR \sin \alpha)}{(QR \sin \alpha)} \right]^2 \sin \alpha \, d\alpha \, dT \quad (2)$$

where η is the volume fraction of particles, $\Delta \rho$ is the scattering length density (SLD) contrast between particles and matrix [38–41], $j_0(x) = \sin(x)/x$, J_1 is the first-order Bessel function. The α is defined as the angle between the cylinder axis and the incident beam [50]. The integral over α averages the form factor over all possible orientations of the disks with respect to scattering vector (Q). The product of $\Delta \rho$ and η can be regarded as a pre-factor. V_p is particle volume ($\pi R^2 T$). The poly-dispersity of the thickness is defined as the variance of the Schulz distribution divided by the mean thickness. Similarly, the SAXS intensity profile of the poly-dispersed rod-like particles have a height T and the Schulz distribution $f(T)$ of thickness (T) can also be calculated according to Equation (2). The SAXS profiles of Samples #1 to #4 can be fitted well using Eqs (1) and (2), as shown in Fig. 4a and b. For clarity, all symbols and abbreviations appearing in the equations are illustrated in Table A1 (Appendix). To correlate mechanical behavior with precipitation kinetics, it is necessary to evaluate the relative volume fraction of GP zones and other strengthening precipitates. Because the value of $\Delta \rho$ is difficult to accurately determined and can be assumed to be a constant, the relative volume fraction can be determined in the SAXS model fitting. Here, the disk-like second-phase particles cause the middle- Q SAXS intensity profile for Samples #1 to #4 are presumed to be Mg_2Si and the corresponding scattering length density (SLD) was calculated in this study to be $1.67 \times 10^{-5} \text{ (\AA}^{-2}\text{)}$. The SLD calculation method was based on previous studies [22, 42]. The high- Q SAXS intensity profile (Samples #1 to #4) is supposedly associated with GP zones. The corresponding SLD, based on its crystallographic composition (AlMg_4Si_6 , space group $C2/m$ [19]), is approximately $1.09 \times 10^{-5} \text{ (\AA}^{-2}\text{)}$. The SLD values of second-phase particles and GP zones during the fitting are assumed to be constant and fixed. Accordingly, the fitted structural parameters and relative volume fractions of precipitates based on the SAXS model are summarized in Tables 2 and 3.

On the other hand, as shown in Fig. 3c and f, the SAXS intensity profiles of Samples #5 and #6 additionally reveal the third shoulder or form factor features between the middle- Q region and high- Q region, located at the Q ranges of $0.050\text{--}0.070 \text{ \AA}^{-1}$ and $0.045\text{--}0.060 \text{ \AA}^{-1}$, respectively. The third shoulder implies the presence of a third type of precipitates with a size in-between second-phase Mg_2Si particles and GP zones. In Sample #5, this third shoulder is primarily attributed to β'' -like (or β'') precipitates with a rod shape, accompanying by (1) the large second-phase Mg_2Si particles producing the middle- Q intensity profile ($0.02 \text{ \AA}^{-1} < Q < 0.05 \text{ \AA}^{-1}$), and (2) GP zones producing the high- Q intensity profile ($0.09 \text{ \AA}^{-1} < Q < 0.35 \text{ \AA}^{-1}$). Alternatively, these findings are consistent with HR-TEM observations, where GP zones and β'' -like phases are observed in the Samples #5, as indicated by orange and blue arrows, respectively in Fig. 5a. In Sample #6, which underwent an additional paint-bake treatment, the shoulder due to the rod-like β'' precipitates shifts toward lower Q region ($0.05 \text{ \AA}^{-1} < Q < 0.07 \text{ \AA}^{-1}$), suggesting the coarsening of β'' precipitates. As shown in Fig. 5b, the HR-TEM image of Sample #6 reveals the presence of GP zones, β''/β' , and θ'/Q' phases. Accordingly, the SAXS profile of Sample #6 (Fig. 4d) shows two shoulders or peaks (form factor) in the middle- Q ($0.02 \text{ \AA}^{-1} < Q < 0.04 \text{ \AA}^{-1}$) and in the high- Q ($0.15 \text{ \AA}^{-1} < Q < 0.25 \text{ \AA}^{-1}$) regions, which are ascribed to disk-like θ'/Q' phases and small rod-like GP zones, respectively. In order to estimate the volume fraction of β''/β' precipitates, the SLD of β''/β' phases was calculated using their nominal composition ($\text{Mg}_5\text{Al}_2\text{Si}_4$) and crystallographic information (monoclinic structure with space group of $C2/m$) [19]. The calculated SLD value is approximately $1.01 \times 10^{-5} \text{ (\AA}^{-2}\text{)}$. Due to the uncertainty in the chemical composition of θ'/Q' phases, their SLDs cannot be reliably calculated and are assumed to be a constant for determining the relative volume fraction. The structure peak is not prominent, the relative volume fraction is relatable rather than the real volume fraction. As a result, the volume fraction of θ'/Q' was not evaluated in the present work. The SAXS profiles for both Samples #5 and #6 are fitted using three models comprising three cylindrical form factors with distinct geometric

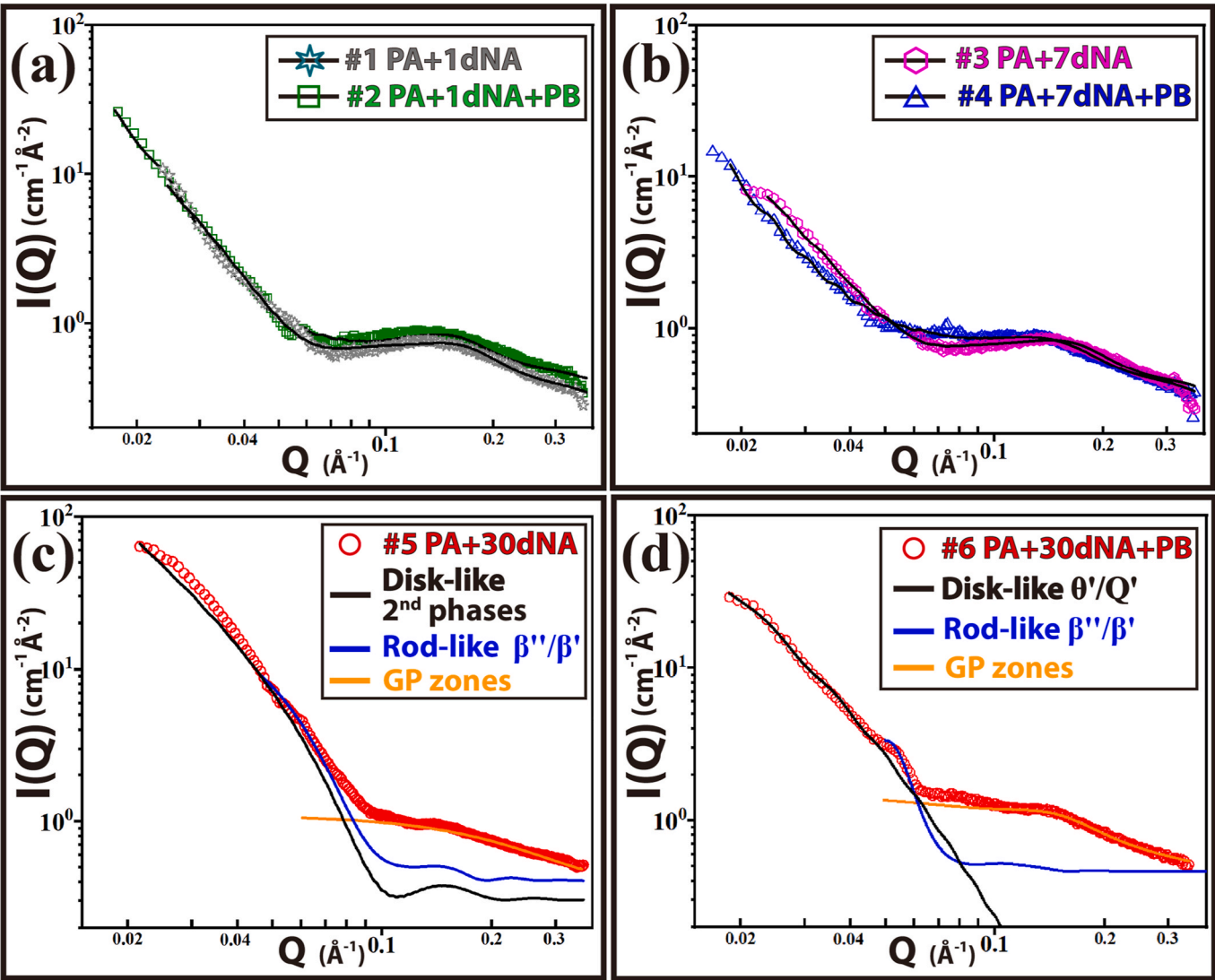


Fig. 4. (a, b) The SAXS profiles of Samples#1 to #4 in comparison with the two model-calculated intensities (solid black curves). (c, d) The SAXS profiles of Samples#5 and #6 in comparison with the three model-calculated intensities (solid black, blue, and orange curves).

Table 2
The evolution in size of the precipitates determined by the SAXS model fitting for Samples #1 to #6.

Treatment	Disk-like second phases		β''-like phases		Rod-like Clusters or GP zones	
	Diameter (nm)	Thickness (nm)	Diameter (nm)	Length (nm)	Diameter (nm)	Length (nm)
#1 PA + 1dNA	234.2	8.9	^a N.A.		1.1	8.5
#2 PA + 1dNA + PB	191.8	11.5	^a N.A.		0.43	16.8
#3 PA + 7dNA	247.4	9.2	^a N.A.		0.47	14.3
#4 PA + 7dNA + PB	161.1	13.4	^a N.A.		0.50	15.6
#5 PA + 30dNA	122.4	7.1	3.8	9.8	0.60	16.0
#6 PA + 30dNA + PB	Disk-like θ'/Q' phases		Rod-like β''/β' phases		Rod-like GP zones	
	Diameter (nm)	Thickness (nm)	Diameter (nm)	Length (nm)	Diameter (nm)	Length (nm)
	49.6	3.6	7.31	21.2	0.72	15.6

^a N.A. is denoted as not indicated.

parameters and a hard-sphere structure factor to account for interparticle correlations [47]. As shown in Fig. 4c and d, the fitting results exhibit good agreement with the experimental data. The model-calculated intensity profiles contributed by three types of particles dominate different Q-regions, as shown in Fig. 4c and d. The corresponding structural parameters are summarized in Tables 2 and 3

3.3. Microstructural characterization

3.3.1. Precursor GP zones

Fig. 6 presents a series of HAADF-STEM micrographs acquired along the [001]_{Al} zone axis, revealing the microstructural evolution of precursor GP zones in Sample #6 (PA + 30dNA + PB). In the early stage

Table 3

The aspect ratio and relative volume fraction of β''/β' precipitates and GP zones determined by the SAXS model fitting for Samples #1 to #6.

Treatment	β'' -like phases or β''/β' phases		Rod-like Clusters or GP zones	
	^a Aspect ratio	Relatively Vol. fraction	^a Aspect ratio	Relatively Vol. fraction
#1 PA + 1dNA	^b N.A.		7.7	0.145
#2 PA + 1dNA + PB	^b N.A.		39.1	0.168
#3 PA + 7dNA	^b N.A.		30.4	0.161
#4 PA + 7dNA + PB	^b N.A.		31.2	0.170
#5 PA + 30dNA	2.58	0.0036	26.7	0.055
#6 PA + 30dNA + PB	2.90	0.0028	21.7	0.014

^a Aspect ratio: Length/Diameter.

^b N.A. is denoted as not indicated.

(Fig. 6a and b), spherical or ellipsoidal GP zones with disordered cluster structures are dispersed within the aluminum matrix. At their interfaces, localized atomic enrichments appear as dot-like bright contrasts (orange arrows in Fig. 6a and b), implying the formation of early-stage GP zones. At the intermediate stage (Fig. 6c), these GP zones exhibit increased structural regularity, with atomic configurations approaching the surrounding FCC lattice. The lateral extension of solute-rich rows becomes evident along the $(020)_{Al}$ habit plane (as indicated by a yellow arrow in Fig. 6c), marking the onset of directional growth. In the mature stage (Fig. 6d and e), GP zones develop into elongated, ordered atomic arrays aligned with the $(020)_{Al}$ planes. The short-range ordered rows (as indicated by yellow arrows in Fig. 6d and e) are observed to initiate at the interfaces and extend into the aluminum matrix, characterized by increased periodicity and regularity. In Fig. 6f, the corresponding FFT pattern reveals additional reflection spots (as indicated by yellow arrows), parallel to the 020_{Al} spot, showing the formation of semi-coherent ordered structures embedded in the matrix.

3.3.2. Sequential transformation of precipitate along dislocations

Figs. 7–9 present a series of HR-TEM micrographs obtained along the $[001]_{Al}$ zone axis, revealing the dislocation-enhanced evolution of solute clusters, GP zones, and early-stage θ'/Q' precipitates in the PB-treated samples as a function of NA duration. In Fig. 7a and b (Sample #2, PA + 1dNA + PB), continuous solute clusters (orange arrow) are aligned along the dislocation line (green arrow), which is oriented in the $[1\bar{1}0]_{Al}$ direction. The corresponding FFT pattern (Fig. 7c), extracted from the region outlined by a white dotted frame (Fig. 7b), shows diffuse scattering near the aluminum matrix spots, indicative of disordered cluster arrangements. In Fig. 7d and e (Sample #4, PA + 7dNA + PB), solute clusters or precursor GP zones are also found along dislocation lines (green arrow) but exhibit a more curved morphology (orange arrow). The corresponding FFT diffractogram shows diffused spots, attributed to the presence of solute clusters or precursor GP zones (framed by a white dotted frame in Fig. 7e), near the aluminum diffraction spots, as shown in Fig. 7f. In Fig. 8a and b, HR-TEM micrographs show another case of dislocation-enhanced precipitation. Solute-depleted or vacant regions (pink arrows in Fig. 8a and b) are observed along dislocation lines and appear to be connected to segmented precipitates. It can be regarded as the dislocation particle-free zones. Moreover, those segmented precipitates grow nearly parallel to the $(020)_{Al}$ habit plane. They are identified as Q'_p and θ'_p precipitates (i.e., the precursor of Q' and θ'), as indicated by orange and white frames, respectively. The corresponding FFT diffractograms of Q'_p and θ'_p phases are provided in Fig. 8c and d, respectively. In Figs. 9 and 10, a series of HR-TEM micrographs taken nearly along the $[001]_{Al}$ zone axis illustrates the microstructural evolution of precipitates along dislocations in Sample #6 (PA + 30dNA + PB condition). As shown in Fig. 9a and c, dislocation lines are clearly observed in the aluminum matrix, serving as

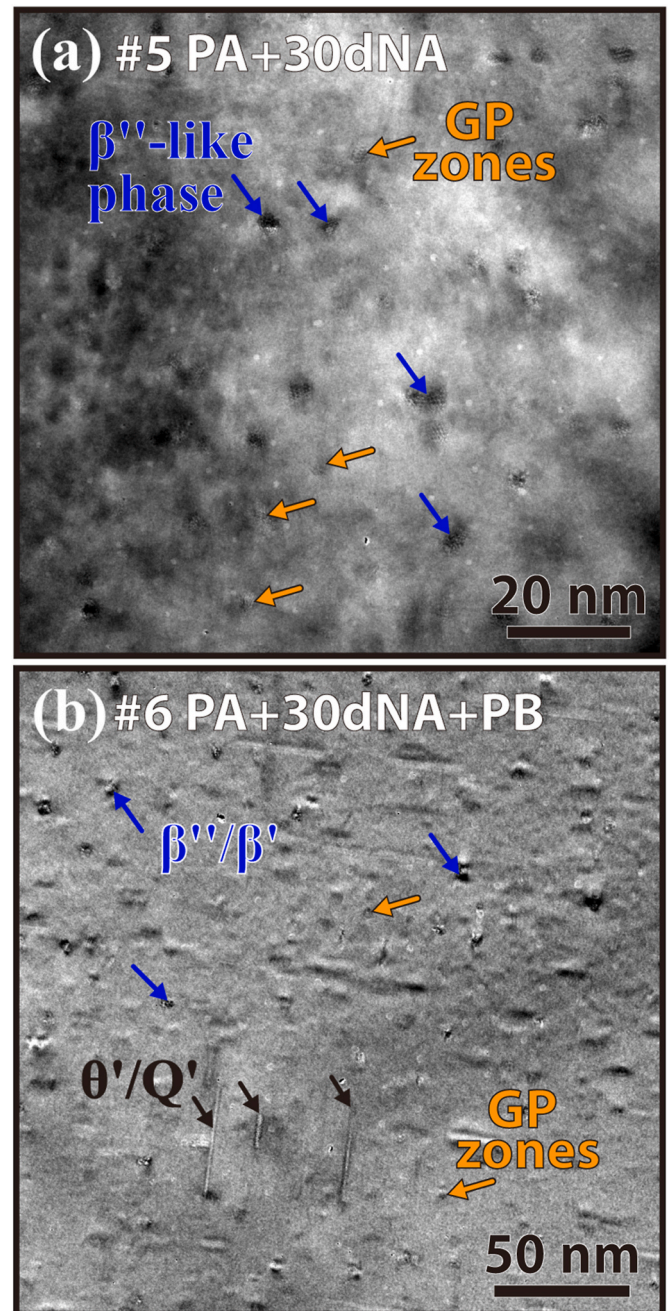


Fig. 5. HR-TEM images showing the formation of GP zones, β'' -like, β''/β' , and θ'/Q' phases in (a) Sample #5 and (b) Sample #6.

potential heterogeneous nucleation sites for precipitates. The corresponding higher-magnification images in Fig. 9b and d reveal the presence of discrete Q' and θ' phases (marked by pink arrows), which are preferentially aligned along the dislocation lines. Those precipitates are sparsely distributed and exhibit a rod-like morphology. Fig. 10a and d, enlarged images of Fig. 9d, reveal the lattice fringe structures of θ' and Q' phases, which are grown along the $(020)_{Al}$ habit plane. The corresponding FFT diffractograms and simulated electron patterns show the orientation relationship of θ' and Q' precipitates in Fig. 10b–c and 10e–f.

4. Discussion

In the following sections, we explored how pre-ageing (PA) and subsequent natural ageing (NA) for 1, 7, and 30 days affect the

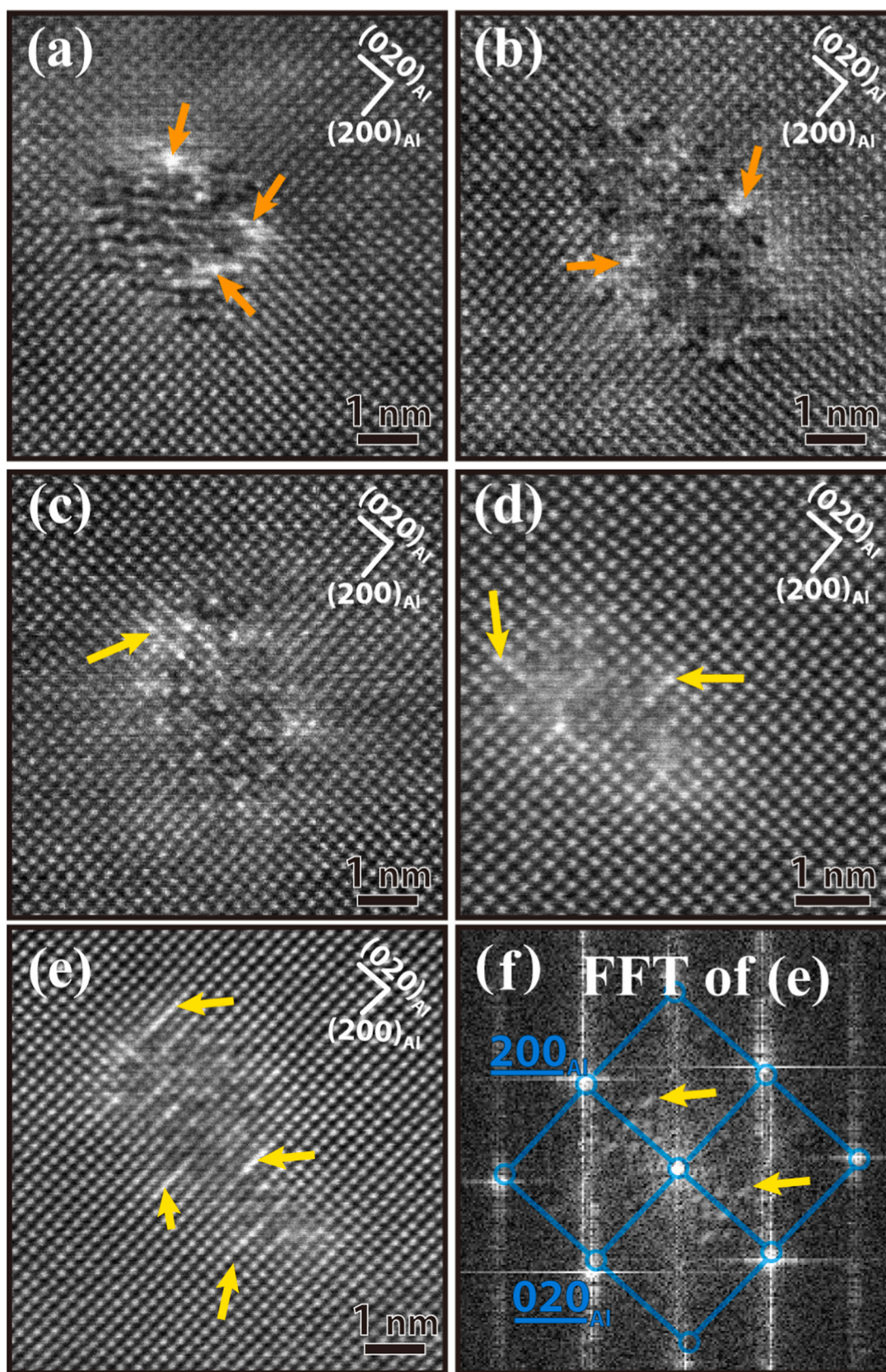


Fig. 6. HAADF-STEM micrographs taken along the $[001]_{Al}$ axis showing the microstructural evolution of GP zones in Sample #6 (PA + 30dNA + PB). (a, b) The initial stage, where bright regions (orange arrows) show the localized atomic enrichment. (c) Intermediate stage, revealing the diffused atomic rows along the $(020)_{Al}$ plane near the interfaces (yellow arrow). (d, e) Intermediate stage, where GP zones evolve into elongated and well-ordered atomic rows that extend inward from interfaces along the $(020)_{Al}$ plane (yellow arrows). (f) The FFT diffractogram of (e) showing the possible orientation relationship between GP zones and aluminum matrix.

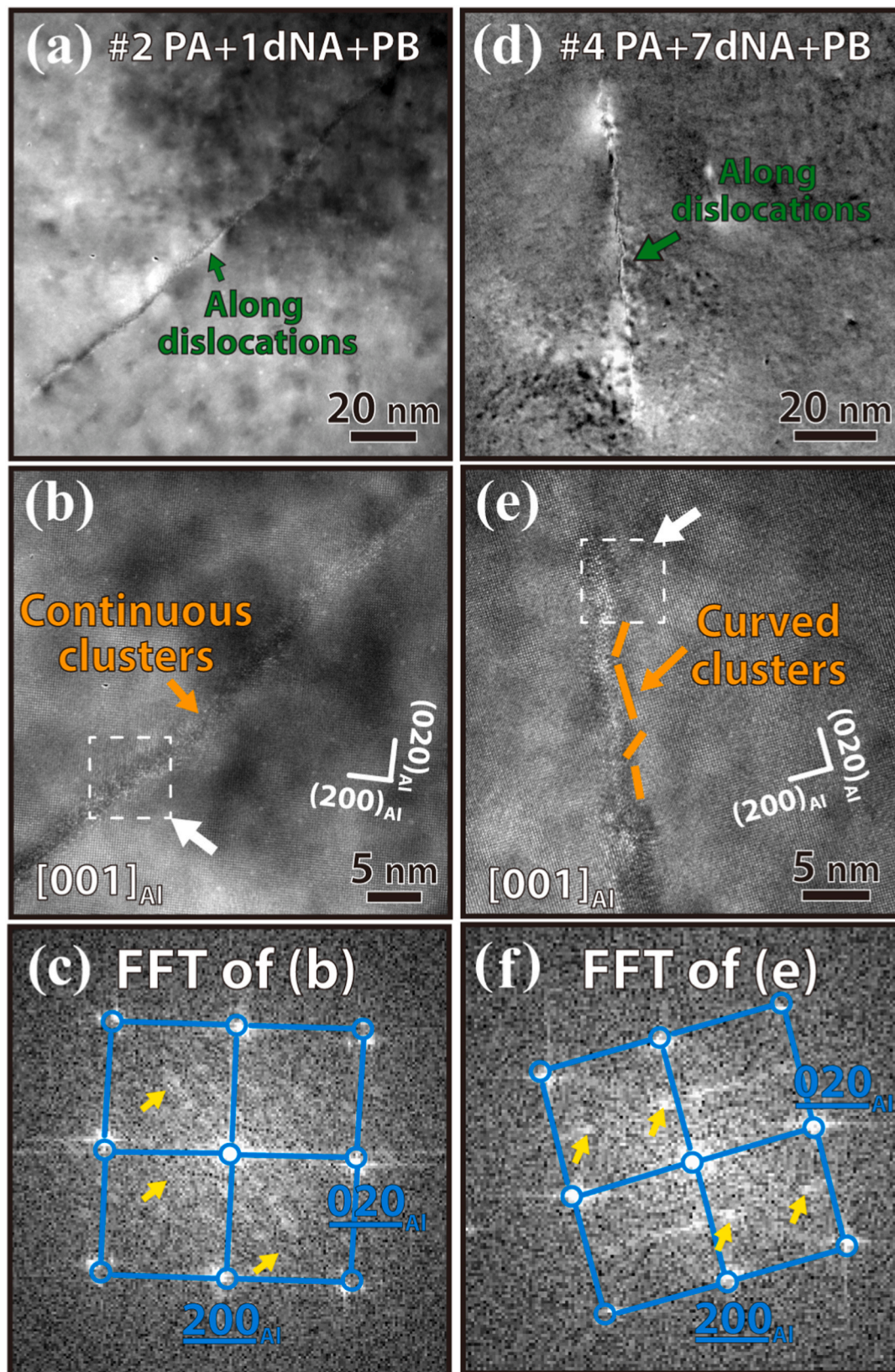


Fig. 7. HR-TEM micrographs taken along the $[001]_{Al}$ zone axis showing the microstructure of solute clusters and GP zones along dislocations. (a, b) In Sample #2 (PA + 1dNA + PB), continuous solute clusters are observed (orange arrow). (c) The corresponding FFT diffractogram (the white dotted frame in (b)) reveals the possible orientation relationship between continuous solute clusters and the aluminum matrix. (d, e) In Sample #4 (PA + 7dNA + PB), curved solute clusters are identified along dislocations (orange arrow). (f) The corresponding FFT diffractogram (the white dotted frame in (e)) shows the possible orientation relationship between curved solute clusters and the aluminum matrix.

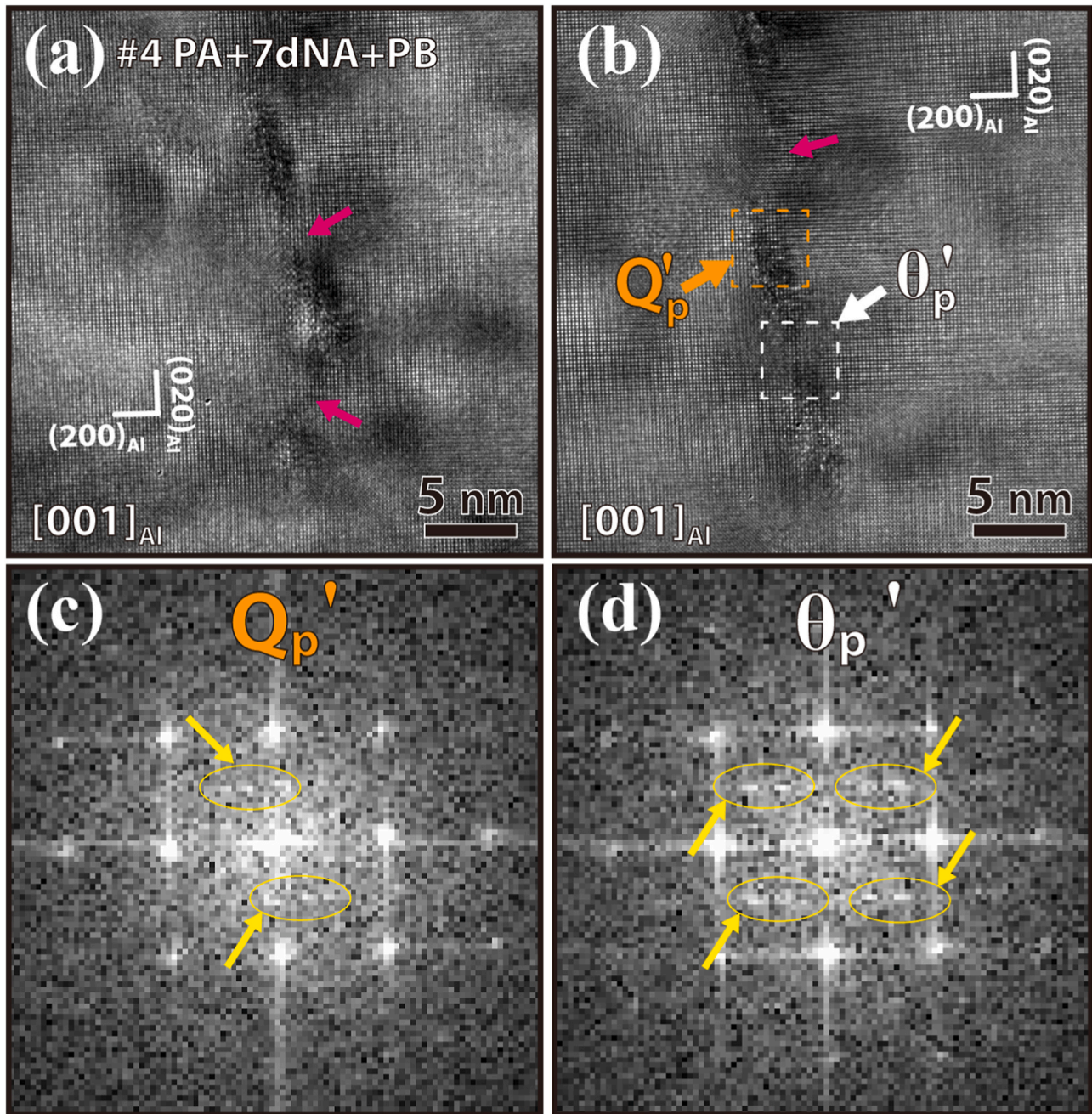


Fig. 8. HR-TEM micrographs taken along the $[001]_{Al}$ zone axis showing the microstructure of segmented precursor precipitates in Sample #4 (PA + 7dNA + PB). (a) The presence of dislocation particle-free zones (pink arrows) is accompanied by the segmented precursor precipitates. (b) Segmented precursor precipitates are observed, designated as Q'_p and θ'_p , and marked by orange and white arrows, respectively. (c, d) The corresponding FFT diffractograms (the orange and white frames in (b)) reveal the possible orientation relationship of Q'_p and θ'_p phases with respect to the aluminum matrix, respectively.

mechanical properties and the coupled precipitation mechanism/kinetics (combination and completion of both concurrently-existing GP zone, β''/β' and θ'/Q' phase transformations) of paint-baked AA6061 alloys. Through SAXS, the precipitation behavior, including the evolution of precipitate size and morphology, was quantitatively determined. The transformation of GP zones and the dislocation-enhanced precipitation of θ'/Q' phase were revealed by HR-TEM and HAADF-STEM. The cumulative ageing impact on the multiphasic co-precipitation of GP zones, β''/β' , and θ'/Q' phases correlated with mechanical properties, including tensile strength, ductility, and work-hardening behavior, has been examined.

4.1. Effect of cumulative ageing on mechanical behavior and precipitation kinetics

The mechanical performance and precipitation behavior of pre-aged AA6061 alloys are markedly influenced by the duration of natural ageing (NA) prior to paint-bake (PB) treatment [11,13]. As summarized in Fig. 2 and Table 1, the strength increases progressively with longer NA duration, both in PB-treated and non-PB treated conditions. Samples #1, #3 to #5 show a steady increase in hardness (from 54 ± 2 HV, 55 ± 3 HV to 64 ± 3 HV), yield strength (from 63 ± 4 MPa, 69 ± 3 MPa to 93 ± 2 MPa), and UTS (from 161 ± 4 MPa, 167 ± 3 MPa to 187 ± 2 MPa), which is attributed to the size and relative volume fraction of GP zones during NA treatment. However, the NA-induced hardening is

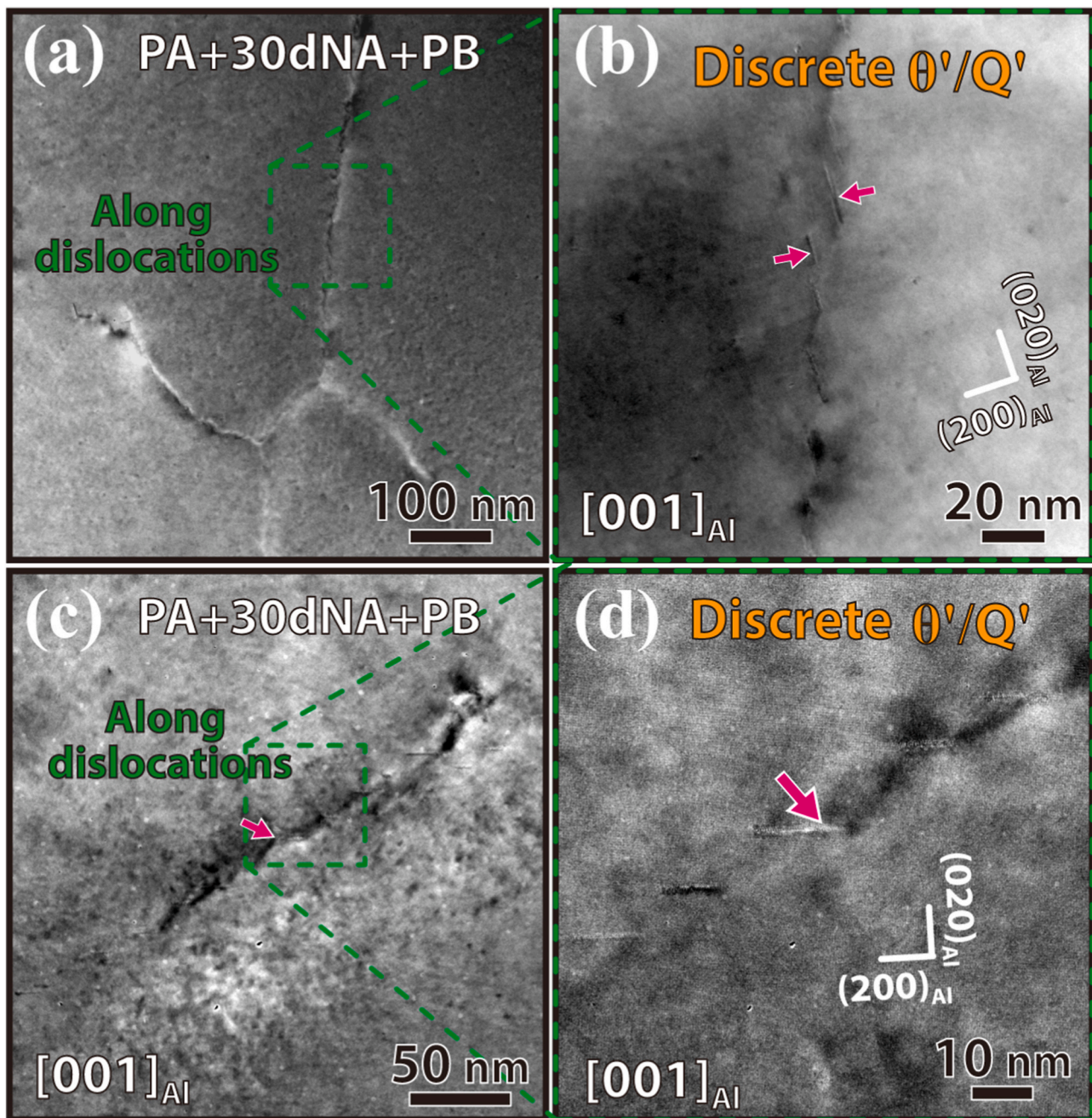


Fig. 9. HR-TEM micrographs taken nearly along the $[001]_{\text{Al}}$ zone axis showing the microstructure evolution of precipitates along dislocations in Sample #6 (PA + 30dNA + PB). (a, c) Low-magnification images reveal the presence of dislocation lines in the aluminum matrix. (b, d) Higher magnification images of the framed regions in (a) and (c), respectively, show the discrete θ'/Q' precipitates aligned along the dislocations.

accompanied by a notable decrease in ductility (from $36.4 \pm 3.1\%$ to $21.7 \pm 2.0\%$), leading to a strength-ductility trade-off. As shown in the SAXS model-fitting results (Tables 2 and 3), the volume fraction of GP zones increases from 0.145 (Sample #1) to 0.161 (Sample #3). Moreover, their average length of GP zones increases from ~ 8.5 nm to ~ 14.3 nm, resulting in a higher aspect ratio from 7.7 (Sample #1) to 30.4 (Sample #3). These results indicate that the longer NA duration (7 days) facilitates the nucleation and growth of GP zones. However, the slight increase in the UTS from 161 ± 4 MPa (Sample #1) to 167 ± 3 MPa (Sample #3) is presumably attributed to the disordered cluster structures of GP zones (Fig. 6a and b), which are hard to inhibit the dislocation movement. Compared to Samples #1 and #3, the prolonged NA condition of 30 days (Sample #5) exhibits a notable increase in UTS to 187 ± 2 MPa (Table 1). Although the size of GP zones (~ 0.6 nm in

diameter and ~ 16.0 nm in length for Sample #5) remains nearly identical to that in Sample #3 (Table 2), the volume fraction significantly decreases to 0.055 (Table 3). This apparent discrepancy between the size stability and volume fraction suggests that the strengthening cannot be attributed only to GP zone evolution. It can be supposed that the prolonged NA (30 days) makes solute atoms in the matrix diffuse preferentially toward pre-existing GP zones, thereby reducing the transformation energy barrier for GP zones and inducing the partial transformation of GP zones into β'' nuclei. This result is consistent with the reported structural evolution of β'' -type GP zones, which undergo sequential transformation through $1\beta''$ eye-like subunits, square-like motifs, binocular configurations, and finally $2\beta''$ eye-like subunits during the natural ageing of 28 days [13]. In Sample #5, the SAXS fitting (Fig. 4c) shows the presence of β'' -like phases with a rod-like

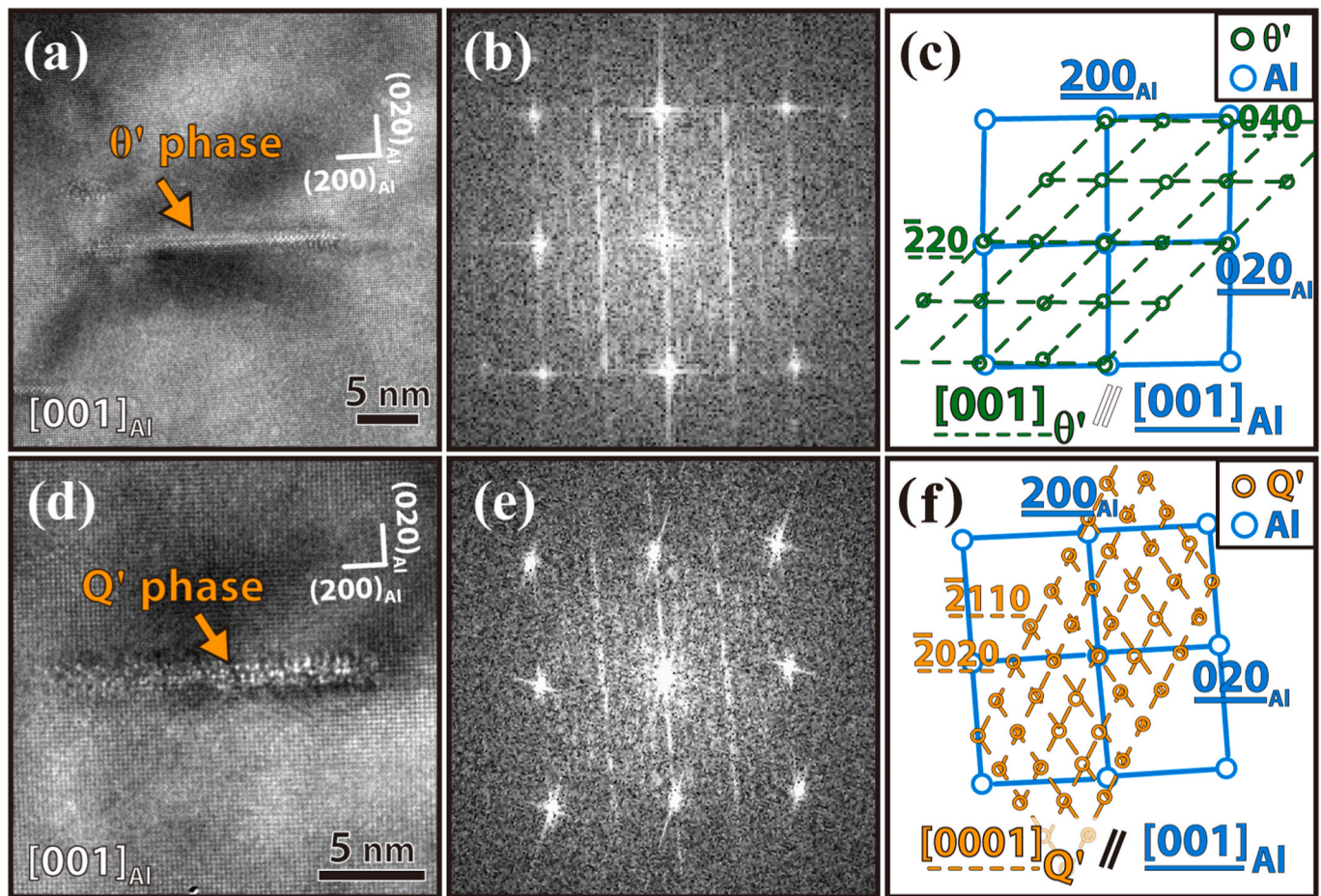


Fig. 10. (a, d) HR-TEM images indicating the structures of θ' and Q' precipitates, grown along the $(020)_{Al}$ habit plane, respectively. (b, e) The corresponding FFT diffraction patterns and simulated electron pattern shows the orientation relationship of θ' precipitate. (c, f) The corresponding FFT diffraction patterns and simulated electron pattern shows the orientation relationship of Q' precipitate.

morphology, having an average length of ~ 9.8 nm and a diameter of ~ 3.8 nm (Table 2), and a relatively low volume fraction of 0.0036 (Table 3). It can be assumed that the Cu addition (0.2 wt%) and the combined effect of PA and prolonged NA enhance the partial transformation from GP zones to β'' -like phases. This suggestion can be referred to the Si/Cu-rich atomic layers spatially isolated within the growth of GP zones to β'' -like phases (as indicated by yellow arrows in Fig. 6c and d). Furthermore, the chemical composition and atomic structure of these β'' -like precipitates will be further verified via atomic-scale EDS and atomic STEM in future investigations.

Upon subsequent PB treatment, each NA condition exhibits a good strengthening response. For example, Sample #2 (PA + 01dNA + PB) exhibits a $\sim 31\%$ increase in UTS compared to its non-PB counterpart (Sample #1). The aspect ratio of rod-like GP zones increases significantly from 7.7 (Sample #1) to 39.1 (Sample #2), accompanied by an increase in the volume fraction from 0.145 to 0.168 (Table 3). This result indicates that in the short-duration NA (1 day) condition, the PB treatment effectively promotes the growth of GP zones along the longitudinal axis and the nucleation of new GP zones. Compared to Samples #3 and #4, the PB treatment slightly increases both the aspect ratio and volume fraction of GP zones from 30.4 to 31.2 and from 0.161 to 0.170, respectively. While the changes in aspect ratio and volume fraction of GP zones are relatively minor, the UTS increases significantly from 167 ± 3 MPa (Sample #3) to 218 ± 3 MPa (Sample #4). This suggests that the combined effect of longer NA (7 days) and PB treatments enhances the structural transformation of GP zones from disordered cluster structures (Fig. 6a and b) to ordered GP zone structures, containing

laterally Si/Cu atomic rows (Fig. 6c), thereby contributing to a higher strengthening effect. Among all samples, Sample #6 (PA + 30dNA + PB) exhibits the highest mechanical strength, with a hardness of 112 ± 2 HV, yield strength of 160 ± 3 MPa, and UTS of 249 ± 4 MPa (Table 1). Compared to Sample #5, the strengthening behavior in Sample #6 occurs without a significant ductility loss ($19.6 \pm 1.5\%$), indicating a well-balanced precipitation microstructure. According to SAXS model fitting (Tables 2 and 3), three types of nanoscale precipitates are identified in this condition: (i) rod-like GP zones (~ 0.72 nm in diameter, ~ 15.6 nm in length, aspect ratio ≈ 21.7), (ii) rod-like β''/β' precipitates (~ 7.31 nm in diameter, ~ 21.2 nm in length, aspect ratio ≈ 2.90), and (iii) disk-like θ'/Q' phases (~ 49.6 nm in diameter, ~ 3.6 nm in length, aspect ratio ≈ 13.8). Despite GP zones and β''/β' precipitates exhibiting relatively low volume fractions, the co-precipitation of GP zones, β''/β' , and θ'/Q' phases suggests a cooperative hardening mechanism. The elongated β''/β' precipitates are presumed to be the primary strengthening phase. In our present work, we have observed the formation of a higher aspect ratio of θ'/Q' precipitates (13.8) along dislocations (Fig. 9), which likely serves as hardening phases. From a thermodynamic perspective, the substantial reduction in GP zone volume fraction from Sample #5 (0.055) to Sample #6 (0.014) suggests extensive transformation during the PB treatment. The redistribution of solute atoms leads to the preferential nucleation and growth of β''/β' along energetically favorable sites, including GP zones and dislocation structures. Moreover, the existence of θ'/Q' phases is associated with the partial transformation of Cu-containing clusters into higher-order precipitates along dislocations, further promoting a stable hardening behavior. This result is consistent

with the presence of Cu-rich solute clusters, which are recognized as precursors to the θ (Al_2Cu) and Q ($\text{Al}_5\text{Cu}_2\text{Mg}_8\text{Si}_6$) phases, as reported in Al-5.70Si-2.06Cu-0.29 Mg (wt.%) aluminum alloys subjected to prolonged NA for about 100 days [11]. To quantitatively elucidate the strength-ductility trade-off, the work-hardening rate behavior (Fig. 2b) provides critical micromechanical insights. Sample #6 exhibits a significantly higher initial work-hardening rate compared to Sample #2, attributed to strong interactions between dislocations and the dense, coexisting rod-like β''/β' and disk-like θ'/Q' precipitates. These barriers increase the probability of Orowan looping and promote rapid dislocation storage upon yielding. However, as strain increases, the work-hardening rate decreases sharply. It indicates that while the dense precipitates initially store dislocations effectively, they also induce high local stress concentrations that accelerate dynamic recovery. Consequently, the work-hardening rate intersects the flow stress curve at a lower strain, limiting the uniform elongation. In contrast, Sample #2 shows a more gradual decline in strain hardening, suggesting sustained dislocation storage capacity. This is facilitated by a larger dislocation mean free path, resulting from the lower fraction and size of precipitates. This prolonged hardening delays the onset of plastic instability, accounting for the superior ductility observed in the short-NA samples.

4.2. Structural evolution of GP zones during prolonged natural ageing

The GP zones in Al–Mg–Si–Cu alloys represent the earliest stage of metastable solute clusters, which are critical in determining the subsequent precipitation sequence and mechanical behavior [13,20]. Their structural evolution during the combined pre-ageing (PA) and prolonged natural ageing (NA) treatments significantly influences precipitation kinetics during the paint-baking (PB) process and the resulting mechanical properties. As shown in Fig. 6a and b, the GP zones exhibit irregular atomic structures with ellipsoidal morphology on the $(001)_{\text{Al}}$ projected plane. These disordered cluster structures are likely to correspond to the microstructures of GP zones formed after PA and short-duration NA (i.e., 1 day, as in Samples #1 and #2). Under these conditions, the aluminum matrix remained supersaturated with solute atoms, and the low-temperature PA treatment at 80 °C for 1 h presumably promotes the nucleation and growth of GP zones. In the previous investigation [20], the structure of β'' -type precursor GP zones, formed during short-term PA at 185 °C for 5 min followed by 30-day NA, consists of multiple eye-shaped atomic subunits. It can be suggested that the evaluated PA temperature enhances the development of a single eye-like configuration in which a central Al atomic column is symmetrically enclosed by alternating Si and Mg columns [20]. During prolonged NA, single eye-like subunits are reported to coalesce into a semi-monoclinic β' -like configuration comprising four or more subunits [20]. That structure is recognized as a stable GP zone [20]. In the present work, disordered GP zones exceeding this critical size are observed, with localized atomic enrichments adjacent to their interfaces. These enrichments (as indicated by orange arrows in Fig. 6a and b), likely consisting of Si- or Cu-rich atomic columns, remain spatially isolated and have not yet transformed into eye-like subunits.

In Fig. 6c, the atomic configurations reveal a transition toward more ordered configurations of GP zones. It can be suggested that multiple Si- or Cu-rich columns, located adjacent to interfaces, begin to laterally coalesce (as indicated by yellow arrows), thereby forming aligned atomic arrays along the $(020)_{\text{Al}}$ habit plane. The laterally atomic rows are interpreted as the early-stage aggregation of eye-like subunits, where individual solute-rich motifs rearrange into coherent chains. Such structures likely represent microstructures formed after PA and intermediate-duration NA (i.e., 7 days, as in Samples #3 and #4). The formation of a single laterally coalesced row may reduce the local interfacial energy by promoting coherent lattice mismatch with the FCC matrix. However, the presence of two or more parallel coalesced rows supposedly increases the locally lattice strain field, thereby facilitating

directional growth of the GP zones and acting as a transformation source for subsequent β'' phases.

As shown in Fig. 6d and e, the well-arranged GP zones, accompanied by laterally coalesced rows, exhibit an elongated and ellipsoidal morphology. This microstructure suggested a transformation pathway in which initially disordered GP zones (Fig. 6a and b) gradually evolve into β'' phases via intermediate, structurally ordered metastable configurations (Fig. 6c), driven by the nucleation-promoting effect of PA and the subsequent growth and ordering by prolonged NA. It can be implied that a fraction of the coalesced atomic rows, which are initially aligned along the $(020)_{\text{Al}}$ habit plane, governs the preferred growth direction and leads to an elongated morphology. Alternatively, along the $(200)_{\text{Al}}$ habit plane, the increased number of coalesced rows likely attracts more solute atoms, thereby minimizing interfacial lattice strain energy. The localized atomic segregation near the interfaces facilitates the nucleation sites of β'' phases. The prolonged NA presumably eliminates the solute accumulation induced by PA and then promotes the structural ordering and directional coalescence of GP zones, evolving from disordered clusters into elongated, metastable configurations. The preferential alignment along the $(020)_{\text{Al}}$ and $(200)_{\text{Al}}$ planes facilitates anisotropic growth and local solute enrichment, providing favorable conditions for subsequent β'' phase transformation during the PB treatment.

4.3. Dislocation-enhanced precipitation of secondary hardening θ'/Q' phases

The presence of dislocations, retained in the aluminum matrix after hot-rolling and solid-solution treatment, plays a pivotal role in facilitating the nucleation and distribution of secondary hardening precipitates during subsequent pre-ageing (PA), natural ageing (NA), and paint-baking (PB) treatments. The series of HR-TEM micrographs presented in Figs. 7–9 reveals the evolution of precipitation along dislocation lines in the PB-treated samples under various natural ageing durations (1, 7, and 30 days). After a short NA and PB (Sample # 2), continuous solute clusters aligned along dislocation lines (Fig. 7a and b) are observed. These dislocation-aligned clusters are short-range ordered structures, presumably acting as precursors of GP zones. It can be suggested that the retained dislocations serve as fast diffusion pathways for the slower-diffusing Cu and Si atoms, resulting in the solute atom segregation. At the intermediate stage of NA (Sample #4), solute atoms, following the PB treatment, progressively rearrange along dislocations, resulting in the transformation of initially continuous clusters into curved and segmented structures. This spatial transition is presumably governed by differences in solute diffusion kinetics and the resulting competitive growth of clusters along different crystallographic planes. In the previous investigations [19,22], the Q' and θ' phases grown on the $\{200\}_{\text{Al}}$ habit planes have been revealed. In this case, it can be assumed that curved clusters, grown along the dislocations and oriented parallel to the similar $(020)_{\text{Al}}$ and $(200)_{\text{Al}}$ habit planes, tend to grow continuously and serve as effective precursors for Q' and θ' phases. On the other hand, the curved clusters, which form along non-parallel $\{200\}_{\text{Al}}$ habit planes, exhibit a lower thermodynamic stability and are more susceptible to dissolution during the PB treatment, eventually leading to solute-depleted or vacant regions along dislocations. As the NA duration is extended to 30 days (Sample #6), this phenomenon of dislocation-enhanced precipitation becomes more pronounced (Fig. 9). Those Q'_p and θ'_p phases, grown along dislocations (Fig. 8), gradually evolve into θ' and Q' phases. The size and spatial distribution are visibly coarser and more distinct. This finding is consistent with existing literature, which suggests that in Al–Mg–Si–Cu alloys, dislocations can facilitate the diffusion of Cu atoms, thereby promoting the co-precipitation of Cu-rich θ' and Q' phases [44]. In the present work, Sample #6 (PA + 30dNA + PB) exhibits the highest yield stress and UTS (Table 1). This significant strengthening effect can be attributed not only

to the formation of β''/β' precipitates in the matrix but also to the additional contribution from these secondary hardening θ'/Q' phases formed on the dislocation network. These strengthening θ'/Q' precipitates, distributed along the dislocation substructures, act as potent obstacles that effectively pin dislocations, impeding their motion during plastic deformation and thereby significantly enhancing the strength and work-hardening capacity. In summary, the dislocation network introduced during hot-rolling processing becomes nucleation sites for secondary hardening θ'/Q' precipitates after a combined ageing treatment involving PA, prolonged NA, and PB. This dislocation-enhanced precipitation mechanism complements the primary strengthening of GP zones and β''/β' precipitates and results in the multiphase co-precipitation strengthening. These factors constitute the key microstructural reason the PA-treated AA6061 alloy retains an excellent bake-hardening response even after extended periods of NA.

5. Conclusion

This study examined the cumulative effect of pre-ageing (PA) and prolonged natural ageing (NA) on the multiphase co-precipitation strengthening behavior of paint-baked AA6061 alloys. Employing a combination of SAXS, TEM, and STEM, we quantitatively characterized the size, morphology, and volume fraction evolution of GP zones, β''/β' precipitates, and θ'/Q' phases. Furthermore, the formation of secondary strengthening θ'/Q' phases along dislocations was observed. This dislocation-enhanced precipitation mechanism of θ'/Q' phases complements the primary strengthening contributions of GP zones and β''/β' phases, leading to significant improvements in tensile strength (249 ± 4 MPa) and elongation ($19.6 \pm 1.5\%$). The key findings of this investigation can be summarized as follows:

1. During short-duration natural ageing (NA) from 1 day to 7 days, rod-like GP zones exhibited pronounced longitudinal growth, with lengths increasing from ~ 8.5 nm to ~ 14.3 nm, accompanied by an increase in their aspect ratio and volume fraction from 7.7 to 39.1 and 0.145 to 0.161, respectively. Following the paint-baked (PB) treatment, the GP-zone fraction further increased slightly (0.168 to 0.170), and their internal structure evolved from disordered clusters (1-day NA) to ordered configurations containing short-range Si/Cu-rich atomic layers aligned with $\{200\}_{Al}$ planes (7-day NA).
2. After prolonged natural ageing (NA) for 30 days, GP zones exhibited increased thermal stability, as evidenced by their maintained sizes (~ 0.60 nm in diameter, ~ 16.0 nm in length) with respect to those in 7-day NA. Specifically, the marked decrease in volume fraction of GP zones represented the transformation of β'' -like precipitates with diameters of ~ 3.8 nm and lengths of ~ 9.8 nm. Subsequent paint-baked (PB) treatment further formed and coarsened the β''/β' phases with sizes reaching ~ 7.31 nm in diameter and ~ 21.2 nm in length.
3. The disk-like θ'/Q' phases, with a size of ~ 49.6 nm in diameter and ~ 3.6 nm in thickness, are observed to nucleate heterogeneously

along dislocations. Initially, solute clusters segregated along dislocation lines and evolved into curved, segmented precursors. Segments aligned with $\{200\}_{Al}$ planes acted as preferential nucleation sites for θ' and Q' , whereas misaligned segments tended to dissolve, leading to particle-free zones along the dislocation.

4. The sequential combination of pre-ageing (PA), prolonged natural ageing (NA), and paint-bake (PB) treatment refined and spatially organized the multiphase microstructure. This structure was characterized by the higher size stability of GP zone rods, elongated β''/β' rods, and high-aspect-ratio θ'/Q' disks, each occupying distinct regions of the matrix and dislocation networks. This spatial and morphological partitioning provided a synergistic co-precipitation strengthening behavior.
5. The sequential precipitation behavior directly influenced the mechanical response. Under non-PB conditions, the UTS progressively increased from 161 ± 4 MPa (1dNA) to 187 ± 2 MPa (30dNA), while elongation decreased from $36.4 \pm 3.1\%$ to $21.7 \pm 2.0\%$, reflecting a strength–ductility trade-off associated with the coarsening and transformation of GP zones into β'' -like precipitates. PB treatment substantially improved both strength and ductility. Specifically, the PA + 30dNA + PB condition achieved a UTS of 249 ± 4 MPa with $19.6 \pm 1.5\%$ elongation. These findings underscore the critical role of multiphase co-precipitation in tailoring the strength–ductility balance in Al–Mg–Si–Cu alloys.

Declaration of competing interest

The authors declare that they have no known competing financial interests or personal relationships that could have appeared to influence the work reported in this paper. This paper was written by authors based on experimental and analytical results. AI tools (such as ChatGPT, Google Gemini or Grammarly) have been used for grammar corrections, but the scientific reasoning, content structure, and interpretations are entirely human-generated.

Acknowledgements

The authors (from Taiwan) wish to express their heartfelt appreciation to the National Science and Technology Council, and the National Center for Instrumentation Research (NCIR) for their generous financial support, as outlined in contracts NSTC 113-2221-E-A49 -030 -MY3, NSTC 114-2221-E-492 -008, and NSTC 114-2811-E-A49 -554. Special gratitude is extended to Dr. Chien-Nan Hsiao (National Center for Instrument Research Institute), Dr. Po-Kai Chiu (National Center for Instrument Research Institute), Dr. Cheng-Si Tsao (National Synchrotron Radiation Research Center), Dr. U. Ser Jeng (National Synchrotron Radiation Research Center), and Dr. Da-Zheng Ou (Department of Materials Science and Engineering at National Yang Ming Chiao Tung University) for their valuable support in TitanTEM, JEOL JEM-F200TEM, and SAXS observation.

Appendix

Table A1

Summary of symbols, parameters, and abbreviations.

Equation	$Q = \frac{4\pi \sin(\theta/2)}{\lambda}$	
Parameters	Q: scattering vector (unit: \AA^{-1}).	Section 2.3 Microstructure characterization
Description	θ : Scattering angle (unit: degree).	
	λ : Incident X-ray wavelength (unit: \AA).	
Equation	$I(Q) = I_{\text{disk}}(Q) + I_{\text{rod}}(Q)$	

(continued on next page)

Table A1 (continued)

Equation	$Q = \frac{4\pi \sin(\theta/2)}{\lambda}$	
Parameters Description	$I(Q)$: Sum of the SAXS intensities contributed by disk-like and rod-like particles. (unit: $\text{cm}^{-1} \text{\AA}^{-2}$) $I_{\text{disk}}(Q)$: The SAXS intensities contributed by disk-like particles (unit: $\text{cm}^{-1} \text{\AA}^{-2}$). $I_{\text{rod}}(Q)$: The SAXS intensities contributed by rod-like particles (unit: $\text{cm}^{-1} \text{\AA}^{-2}$).	Section 3.2 Quantitative structural characterization of precipitates
Equation	$I_{\text{disk/rod}}(Q) = \eta \Delta\rho^2 / V_p^2 S(\eta, Q) f(T) j_0 \left(Q \frac{T}{2} \cos \alpha \right)^2 \left[\frac{2J_1(QR \sin \alpha)}{(QR \sin \alpha)} \right]^2 \sin \alpha \alpha \, d\alpha \, dT$	
Parameters Description	$I_{\text{disk/rod}}(Q)$: The SAXS intensities contributed by disk-like or rod-like particles (unit: $\text{cm}^{-1} \text{\AA}^{-2}$). Q : scattering vector (unit: \AA^{-1}). η : The volume fraction of particles (dimensionless). $\Delta\rho$: The scattering length density (unit: \AA^{-2}). V_p : The particle volume ($\pi R^2 T$ or $\pi R^2 L$) (unit: \AA^3). R : The radius of particles (unit: \AA). T/L : The thickness (T) of disk-like particles (unit: \AA). The length (L) of rod-like particles (unit: \AA). $S(\eta, Q)$: Schultz size distributions and hard-sphere structure factor. $f(T)$: Schulz distribution of thickness for disk-like particles. $f(L)$: Schulz distribution of length for rod-like particles. $j_0(x)$: $\sin(x)/x$, the zeroth-order spherical Bessel function (dimensionless), with $x = Q T/2 \cos \alpha$ or $Q L/2 \cos \alpha$. $j_1(x)$: The first-order Bessel function (dimensionless), with $x = Q R \sin \alpha$. α : The angle between the cylinder axis and the incident beam (unit: degree).	Section 3.2 Quantitative structural characterization of precipitates

References

[1] Zhu S, Shih H-C, Cui X, Yu C-Y, Ringer SP. Design of solute clustering during thermomechanical processing of AA6016 Al–Mg–Si alloy. *Acta Mater* 2021;203:116455.

[2] Yang Z, Cheng J, Liang Z, Banhart J. Two-step preaging of an al–mg–si alloy. *Adv Eng Mater* 2022;2200973:1.

[3] Yin Z, Liu C, Ma P, Yang J. Enhancing strength-ductility synergy in age-hardened Al-Mg-Si alloy via combined pre-ageing and pre-straining. *J Alloys Compd* 2025;1010:178264.

[4] Duan S, Lu Y, Ke X, Huang C, Du J, Fu N, Xu Y, Yan Y. Enhancement of bake-hardening response and mechanical properties in AA6111 alloy via synergistic pre-aging and pre-straining treatments. *J Alloys Compd* 2025;182986.

[5] Saruwatari N, Yasue K, Nakayama Y. Effect of reheating after low temperature pre-aging on microstructure of 6061 Al–Mg–Si alloy. *Mater Trans* 2022;63:286.

[6] Schmid F, Dumitraschkewitz P, Kremmer T, Uggowitzer PJ, Tosone R, Pogatscher S. Enhanced aging kinetics in Al-Mg-Si alloys by up-quenching. *Commun Mater* 2021;2(1):58.

[7] Arnoldt A, Semmelrock L, Soukup D, Österreicher JA. Analysis of second phase particles in metals using deep learning: segmentation of nanoscale dispersoids in 6xxx series aluminum alloys (Al-Mg-Si). *Mater Char* 2022;191:112138.

[8] Li Z, Qin J, Zhang H, Wang X, Zhang B, Nagaumi H. Improved distribution and uniformity of α -Al(Mn,Cr)Si dispersoids in al-mg-si-cu-mn (6xxx) alloys by two-step homogenization. *Metall Mater Trans A* 2021;52:3204.

[9] Remøe MS, Westermann I, Marthinsen K. Characterization of the density and spatial distribution of dispersoids in Al-Mg-Si alloys. *Metals* 2018;9:26.

[10] Aruga Y, Kozuka M, Takaki Y, Sato T. Evaluation of solute clusters associated with bake-hardening response in isothermal aged Al-Mg-Si alloys using a three-dimensional atom probe. *Metall Mater Trans A* 2014;45(13):5906.

[11] Lee S-H, Seo N, Kang M, Son SB, Lee S-J, Jung J-G. Natural aging-induced nanoprecipitation and its impact on tensile properties of Al–Si–Cu–Mg cast alloy. *Mater Char* 2024;215:114204.

[12] Serizawa A, Hirose S, Sato T. Three-dimensional atom probe characterization of nanoclusters responsible for multistep aging behavior of an Al-Mg-Si alloy. *Metall Mater Trans A* 2008;39(2):243.

[13] Marioara CD, Andersen SJ, Hell C, Frafjord J, Friis B, Bjørge R, Ringdalen IG, Engler O, Holmestad R. Atomic structure of clusters and GP-zones in an Al-Mg-Si alloy. *Acta Mater* 2024;269:119811.

[14] Li G, Guo M, Du J, Zhuang L. Synergistic improvement in bake-hardening response and natural aging stability of Al-Mg-Si-Cu-Zn alloys via non-isothermal pre-aging treatment. *Mater Des* 2022;218:110714.

[15] Fu L, Ma P, He J, Liu C. Reversion ageing and subsequent age hardening response in T4 tempered AA6016 alloy. *J Alloys Compd* 2025;1022:179874.

[16] Du Q, Tang K, Marioara CD, Andersen SJ, Holmedal B, Holmestad R. Modeling over-ageing in Al-Mg-Si alloys by a multi-phase CALPHAD-coupled Kampmann-Wagner numerical model. *Acta Mater* 2017;122:178.

[17] Andersen SJ, Marioara CD, Visser R, Frøseth A, Zandbergen HW. The structural relation between precipitates in Al–Mg–Si alloys, the Al-matrix and diamond silicon, with emphasis on the trigonal phase U1-MgAl2Si2. *Mater Sci Eng* 2007;444(1):157.

[18] Saito G, Sano Y, Mizuno K, Torigoe S, Takata K, Okajima T, Muto S. Precipitation behavior during low-temperature aging in Al–Mg–Si alloy using STEM-EDS intensity correlograms. *Mater Sci Eng* 2025;923:147686.

[19] Faregh SM, Larouche D, Chen XG. Atomic scale characterization of precipitates in an Al-Si-Mg alloy containing excess Si and trace amounts of Cu. *Mater*, 40; 2025, 102396.

[20] Li C, Marioara CD, Hatzoglou C, Andersen SJ, Holmestad R, Li Y. Accelerating precipitation hardening by natural aging in a 6082 Al-Mg-Si alloy. *Acta Mater* 2024;281:120396.

[21] Zheng J-H, Dong Y, Zheng K, Dong H, Lin J, Jiang J, Dean TA. Experimental investigation of novel fast-ageing treatments for AA6082 in supersaturated solid solution state. *J Alloys Compd* 2019;810:151934.

[22] Yeh C-W, Chen C-J, Tai C-L, Yang Y-L, Misra RDK, Hsiao C-N, Chen C-C, Tsao C-S, Jeng U, Lin H-C, Chung T-F. Pre-aged and paint-baked strengthening response on the prolonged natural-aged al-mg-si-cu aluminum alloys. *J Alloys Compd* 2024;1008:176677.

[23] Chung T-F, Yang Y-L, Huang B-M, Shi Z, Lin J, Ohmura T, Yang J-R. Transmission electron microscopy investigation of separated nucleation and in-situ nucleation in AA7050 aluminium alloy. *Acta Mater* 2018;149:377.

[24] Chung T-F, Yang Y-L, Shiojiri M, Hsiao C-N, Li W-C, Tsao C-S, Shi Z, Lin J, Yang J-R. An atomic scale structural investigation of nanometre-sized η precipitates in the 7050 aluminium alloy. *Acta Mater* 2019;174:351.

[25] Chung T-F, Yang Y-L, Tai C-L, Shiojiri M, Hsiao C-N, Tsao C-S, Li W-C, Shi Z, Lin J, Chena H-R, Yang J-R. HR-STEM investigation of atomic lattice defects in different types of η precipitates in creep-age forming Al–Zn–Mg–Cu aluminium alloy. *Mater Sci Eng* 2021;815:141213.

[26] Roven HJ, Liu M, Werenskiold JC. Dynamic precipitation during severe plastic deformation of an Al–Mg–Si aluminium alloy. *Mater Sci Eng* 2008;483–484:54.

[27] Babu V, Shanmugavel BP, Padmanabhan KA. On the role of semi-die angle in multi-pass cyclic expansion extrusion: effects on microstructure and mechanical properties of AA 6063. *Met Mater Int* 2023;29(10):3066.

[28] Chung T-F, Yeh C-W, Liaw Y-S, Lin J-R, Ho P-L, Hsiao C-N, Tsao C-S, Chou C-M, Yang Y-L, Yang J-R, Chen C-Y, Hong W. Grain structure and co-precipitation behavior of high-Zn containing Al–Zn–Mg–Cu aluminium alloys during deformation via high-temperature upsetting-extrusion. *J Alloys Compd* 2023;968:171871.

[29] Shamas UD, Kamran J, Hasan BA, Tariq NH, Mehmood M, Shamas uz Zuha M. Effect of thermo mechanical treatments and aging parameters on mechanical properties of Al–Mg–Si alloy containing 3wt.% Li. *Mater Des* 2014;64:366.

[30] Serizawa A, Sato T, Miller MK. Effect of cold rolling on the formation and distribution of nanoclusters during pre-aging in an Al–Mg–Si alloy. *Mater Sci Eng* 2013;561:492.

[31] Liu M, Guo Q, Zhao J, Liu Z, Chen K, Cao Y, Chen T, Qian F, Pan S, Cao X, Zhao H, Sha G, Yang Z, Banhart J, Zhao P. Modulated clustering and precipitation in an Al–Mg–Si alloy AA 6014 via enhanced pre-aging. *Acta Mater* 2025;296:121164.

[32] Duan S, Lu Y, Li A, Tang M, Chen W, Huang C, Du J, Xu Y, Yan Y. Synergistic effect of Cu addition and pre-straining on the natural aging and artificial age-hardening behavior of AA6111 alloy. *Mater* 2025;18(7):1635.

[33] Lai YX, Fan W, Yin MJ, Wu CL, Chen JH. Structures and formation mechanisms of dislocation-induced precipitates in relation to the age-hardening responses of Al-Mg-Si alloys. *J Mater Sci Technol* 2020;41:127.

- [34] DiCecco S, Di Ciano M, Baghbanaghaie N, Esmaeili S, Wells M, Worswick M. Warm aging of pre-aged AA6013 sheet and its relevance to room temperature and warm forming applications—experimental and modeling analyses. *J Mater Eng Perform* 2023;32(21):9797.
- [35] Chung T-F, Yang Y-L, Hsiao C-N, Li W-C, Huang B-M, Tsao C-S, Shi Z, Lin J, Fischione PE, Ohmura T, Yang J-R. Morphological evolution of GP zones and nanometer-sized precipitates in the AA2050 aluminium alloy. *Int J Lightweight Mater Manuf* 2018;1:142.
- [36] Chen K, Liu C, Ma P, Yang J, Zhan L, Huang M, Hu J. Enhancing creep formability and comprehensive property in Al–Mg–Si alloy by combinatorial pre-ageing and large pre-deformation. *Mater. Sci. Eng. A* 2021;826:141967.
- [37] Zou Y, Cao L, Wu X, Tang S, Guo M. Synergetic effect of natural ageing and pre-stretching on the ageing behavior in T'/η' phase-strengthened Al–Zn–Mg–Cu alloys. *J Mater Sci Technol* 2023;146:240.
- [38] Zhou P, Song Y, Lu J, Hua L, Wu W, Sun Q, Su J. Novel fast-aging process for Al–Zn–Mg–Cu alloy sheets and its micro-mechanisms. *Mater Sci Eng* 2022;856:143996.
- [39] Liu Y, Zhu B, Wang Y, Li S, Zhang Y. Fast solution heat treatment of high strength aluminum alloy sheets in radiant heating furnace during hot stamping. *Int J Lightweight Mater Manuf* 2020;3(1):20.
- [40] Adamczyk-Cieslak B, Mizera J, Kurzydowski KJ. Microstructures in the 6060 aluminium alloy after various severe plastic deformation treatments. *Mater Char* 2011;62(3):327.
- [41] Ren D, Wang C, Wei X, Zhang Y, Han S, Xu W. Harmonizing physical and deep learning modeling: a computationally efficient and interpretable approach for property prediction. *Scr Mater* 2025;255:116350.
- [42] Fu Y, Yousefi Mehr V, Toroghinejad MR, Chen X, Jie J, Zhu S. Twinning and stacking fault-induced precipitation in an aluminum alloy. *J Mater Res Technol* 2025;34:2127.
- [43] Qian D, Chen J, Luo H, Wang F, Hua L. Electric current-induced directional slip of dislocation and grain boundary ordering. *materials today advances*, 24; 2024, 100530.
- [44] Gazizov MR, Zuiko IS, Holmestad R, Gazizova MY, Kaibyshev RO. Particle morphology characterization in an over-aged Al–Cu–Mg–Si alloy using TEM. *Mater Char* 2024;211:113923.
- [45] Tsao C-S, Chen C-Y, Jeng U-S, Kuo T-Y. Precipitation kinetics and transformation of metastable phases in Al–Mg–Si alloys. *Acta Mater* 2006;54:4621.
- [46] Chien C, Tsao C-S, Wu S-K, Chang C-Y, Chang P-C, Kuo Y-K. Characteristics of the strain glass transition in as-quenched and 250 °C early-aged Ti48.7Ni51.3 shape memory alloy. *Acta Mater* 2016;120:159.
- [47] Tsao C-S, Huang EW, Wen M-H, Kuo T-Y, Jeng S-L, Jeng US, Sun Y-S. Phase transformation and precipitation of an Al–Cu alloy during non-isothermal heating studied by in situ small-angle and wide-angle scattering. *J Alloys Compd* 2013;579:138.
- [48] Londoño OM, Tancredi P, Rivas P, Muraca D, Socolovsky LM, Knobel M. Small-angle X-ray scattering to analyze the morphological properties of nanoparticulated systems. In: *Handbook of materials characterization*. City: Springer; 2018. p. 37.
- [49] Guinier A, Fournet G. *Small angle scattering*. first ed. City: John Wiley and Sons; 1955. p. 211–3.
- [50] Kinning DJ, Thomas EL. Hard-sphere interactions between spherical domains in diblock copolymers. *Macromolecules* 1984;17(9):1712.